Research Square

Preprints are preliminary reports that have not undergone peer review.
They should not be considered conclusive, used to inform clinical practice,
or referenced by the media as validated information.

Structural and functional dissection of ASCT2 interaction with Syncytin-1 mediating cell-cell fusion

Dirk Slotboom

d.j.slotboom@rug.nl

University of Groningen https://orcid.org/0000-0002-5804-9689

Anna Borowska

University of Groningen https://orcid.org/0000-0003-4127-3497

Krystof Stafl

Institute of Molecular Genetics of the Czech Academy of Sciences https://orcid.org/0000-0001-8708-606X

Michal Sýkora

Institute of Molecular Genetics https://orcid.org/0000-0001-8049-0748

Jan Rheinberger

University of Groningen https://orcid.org/0000-0002-9901-2065

Martin Travnicek

Institute of Molecular Genetics of the Czech Academy of Sciences https://orcid.org/0000-0003-0627-2560

Lubomira Pecnova

Institute of Molecular Genetics of the Czech Academy of Sciences

Anna Janovska

Institute of Organic Chemistry and Biochemistry of the Czech Academy of Sciences https://orcid.org/0009-0004-0353-8225

Jiri Hejnar

Institute of Molecular Genetics of the Czech Academy of Sciences

Cristina Paulino

Heidelberg University https://orcid.org/0000-0001-7017-109X

Katerina Trejbalova

Institute of Molecular Genetics of the Czech Academy of Sciences https://orcid.org/0000-0002-9872-3041

Article

Keywords:

Posted Date: June 24th, 2026

DOI: https://doi.org/10.21203/rs.3.rs-9860868/v1

License: This work is licensed under a Creative Commons Attribution 4.0 International License.
Read Full License

Additional Declarations: There is **NO** Competing Interest.

Structural and functional dissection of ASCT2 interaction with Syncytin-1 mediating cell-cell fusion

Anna M. Borowska[1*], Krystof Stafl[2*], Michal Sykora[3*], Jan Rheinberger[1,4], Martin Travnicek[2], Lubomira Pecnova[2], Anna Janovska[5], Jiri Hejnar[2], Cristina Paulino[1,4], Dirk J. Slotboom[1†], Katerina Trejbalova[2†]

[1]Faculty of Science and Engineering, Groningen Biomolecular Sciences and Biotechnology, Membrane Enzymology Group, University of Groningen, 9727 AG, Groningen, the Netherlands

[2]Institute of Molecular Genetics of the Czech Academy of Sciences, Laboratory of Viral and Cellular Genetics, Videnska 1083, 14220 Prague, Czech Republic

[3]Institute of Structural and Molecular Biology, Division of Biosciences, University College London, Gower Street, London, WC1E 6BT, United Kingdom

[4]Biochemistry Center Heidelberg, Heidelberg University, Im Neuenheimer Feld 328, 69120 Heidelberg, Germany

[5]Institute of Organic Chemistry and Biochemistry of the Czech Academy of Sciences, Flemingovo namesti 2, 16610 Prague, Czech Republic

*These authors contributed equally to this work.

[†]Email: d.j.slotboom@rug.nl, katerina.trejbalova@img.cas.cz

Abstract

ASCT2 is a neutral amino acid transporter that also serves as the cellular receptor for Syncytin-1, a retroviral envelope gene co-opted for placentation in humans. Although the closely related transporter ASCT1 shares high sequence similarity and the same trimeric architecture, it does not support Syncytin-1–mediated cell–cell fusion, and the molecular basis of receptor specificity has remained unresolved. Here, we determine the cryo-EM structure of the ASCT2-Syncytin-1 complex and show that Syncytin-1 binds ASCT2 in its outward-oriented state with high affinity and slow dissociation. Biochemical analyses demonstrate that receptor engagement reduces, but does not abolish, glutamine transport. This residual transport activity arises from an asymmetric binding mode of Syncytin-1, in which one protomer of ASCT2 retains conformational freedom to facilitate transport. Structure-guided mutagenesis combined with cell-based functional assays shows that Syncytin-1 recognition depends on the combined contribution of multiple extracellular determinants rather than on individual critical residues. Among the ASCT2 variants tested, receptor function was abolished only in mutants that simultaneously lost transporter activity. This extensive interaction interface likely contributes to the robustness of receptor engagement in a physiological context. Consistent with this model, Syncytin-1 sensitivity to ASCT1 requires multiple substitutions distributed across three different extracellular loops. Together, these findings establish how Syncytin-1 exploits the conformational dynamics, trimeric architecture, and extensive interaction interface of ASCT2 to enable receptor-specific membrane fusion while preserving transporter activity, providing a structural and functional framework for receptor specificity within the SLC1 family.

Introduction

Endogenous retroviruses (ERVs) account for approximately 8% of the human genome and represent remnants of ancient retroviral infections that integrated into the germline and became fixed in ancestral populations during evolution[1]. Over time, most ERV sequences acquired mutations or deletions and became non-functional; however, a subset of ERV-derived genes underwent positive selection and were co-opted by the host to perform key physiological functions. A striking example is Syncytin-1 that evolved from the envelope glycoprotein of human ERV type W (HERV-W)[2]. Syncytin-1 is expressed from a specific HERV-W locus active exclusively in the placenta[3,4], where it mediates the fusion of cytotrophoblast cells to form the multinucleated syncytiotrophoblast layer[5], a specialized tissue essential for embryo implantation and maternal-fetal exchange of nutrients and gases. The critical role of syncytin-mediated cell fusion in placental development is conserved across mammals, although different mammalian lineages have independently co-opted distinct ERV envelope genes for this purpose. The functional importance of syncytins in syncytiotrophoblast differentiation has been demonstrated in mouse models[6–8].

At the molecular level, Syncytin-1 is a gamma-type retroviral envelope protein that assembles into homotrimers. During maturation, each protomer is proteolytically cleaved into the surface (SU) and transmembrane (TM) subunits, which remain covalently linked via a disulfide bond (**Supplementary Fig. 1a**)[9]. The SU subunit contains the receptor-binding domain (RBD), conferring specificity for a cellular receptor, while the TM subunit, comprising the fusion peptide and membrane-anchoring helix, mediates membrane fusion. During cell-cell fusion, Syncytin-1 binding to its receptor is thought to trigger isomerization of the intersubunit disulfide bond, enabling the SU dissociation and exposure of the fusion peptide on the TM, as a first step of membrane fusion.

Phylogenetic analyses show a close evolutionary relationship between Syncytin-1 and the envelope proteins of feline endogenous retrovirus RD114, Mason-Pfizer monkey virus (MPMV), and squirrel monkey retrovirus (SMRV)[10]. These retroviruses, together with Syncytin-1, use the same cellular receptor and are therefore classified within the RD114/type D interference group (RDR)[11]. The receptor was identified as SLC1A5 (ASCT2), a Na^+-dependent neutral amino acid transporter in the SLC1 family[12–14]. ASCT2 is broadly expressed in the kidney, lung, brain, and placenta, and mediates the transport of neutral amino acids, including alanine, serine, threonine, and glutamine[15,16]. Thus, ASCT2 serves both as a viral receptor and a cellular transporter, raising a fundamental question: how receptor engagement affects the transporter function.

ASCT2 forms a homotrimer, with each subunit transporting amino acids independently[17,18]. Each protomer contains a scaffold domain that contacts other subunits and a transport domain that undergoes elevator-like movements between outward- and inward-facing conformations to translocate substrate[19]. Each ASCT2 protomer contains five extracellular loops (ECL1–ECL5) that connect the transmembrane helices (TM) and shape the extracellular surface of the transporter (**Supplementary Fig. 1b**). Previous structural work has proposed a poorly conserved extracellular β-strand region within the scaffold domain as a potential recognition site for Syncytin-1[20]. A recent cryo-EM structure of the ASCT2-Syncytin-1 complex further revealed a clamp-like recognition mechanism in which the Syncytin-1 RBD specifically recognizes the trimeric fold of ASCT2 and forms a hybrid β-sheet with ECL2[21]. However, this structural snapshot does not explain how individual features of the interface contribute to receptor recognition in a cellular context, whether they

act cooperatively, and how receptor engagement impacts amino acid transport. In particular, it remains unclear whether Syncytin-1 binding is compatible with the conformational dynamics required for amino acid exchange or instead perturbs the physiological function of ASCT2. In addition, the closely related transporter ASCT1, despite high structural similarity to ASCT2[22], does not act as a receptor for Syncytin-1[23], raising the question of how recognition selectivity is achieved.

Here, we combine cryo-EM structural analysis with biochemical and cell-based functional assays to define the molecular basis of Syncytin-1 recognition by ASCT2. Our results reveal that receptor engagement is strongly dependent on ASCT2 adopting an outward-facing conformation, demonstrate that Syncytin-1 binding modulates – but does not abolish – ASCT2 transport activity, and identify the structural features that collectively define receptor specificity for Syncytin-1.

Results

Syncytin-1 selectively recognizes an outward-facing ASCT2 conformation

To investigate the molecular interaction between Syncytin-1 and its receptor ASCT2, we generated a secreted form of Syncytin-1, hereafter referred to as S1-RBD, containing the RBD stabilized by fusion with the Fc region of monomeric rabbit IgG[23,24] (**Supplementary Fig. 1c**). Using this construct, we determined a cryo-EM structure of S1-RBD in complex with wild-type ASCT2 purified in glyco-disogenin (GDN) detergent in the presence of glutamine (**Supplementary Fig. 2a**). After 3D classification, we obtained a 2.9 Å resolution map with well-defined density for all three ASCT2 protomers and the bound S1-RBD, enabling confident model building and detailed structural analysis (**Fig. 1a**, **Supplementary Fig. 3**, **Supplementary Table 1**). The structure reveals a single S1-RBD occupying the extracellular aqueous basin at the center of the ASCT2 trimer, adopting an elongated shape with its long axis parallel to the membrane plane (**Fig. 1a**). While the overall binding mode closely resembles that observed in a previously reported structure of the ASCT2-Syncytin-1 complex[21], a key distinction lies in the global conformation of ASCT2: all three transport domains adopt the outward-facing states (**Fig. 2a**). This contrasts with the previous structure in which one protomer was inward-facing while the others were outward-facing.

The structural observations suggest that S1-RBD recognition of ASCT2 requires that the transporter be able to adopt outward-facing conformations of at least two of its protomers. To test this hypothesis, we sought to experimentally bias ASCT2 toward defined conformations using detergent conditions known to stabilize distinct states. ASCT2 purified in DDM:CHS detergent, which favors all protomers in the inward-facing conformation[19,25], failed to form a detectable *in vitro* complex when using S1-RBD as bait in pull-down assays (**Supplementary Fig. 2b**). In contrast, when ASCT2 was purified in GDN detergent, which stabilizes a symmetric outward-facing conformation (**Supplementary Fig. 4, Supplementary Table 1**), robust co-elution of ASCT2 with S1-RBD was observed in pull-down assays (**Supplementary Fig. 2c**).

To quantitatively assess this conformational dependence, we measured binding kinetics using grating-coupled interferometry (GCI). S1-RBD was immobilized on a Protein G-functionalized chip surface via its Fc domain (**Supplementary Fig. 5a**), and purified ASCT2 solubilized in different detergents was injected. GDN-solubilized ASCT2 exhibited concentration-dependent binding with rapid association and slow dissociation kinetics, corresponding to high-affinity interaction with a K_D value in the nanomolar range (<10 nM) (**Fig. 1b, Supplementary Fig. 5b,c**). In contrast, ASCT2 solubilized in DDM:CHS showed an approximately 10-fold reduced binding response (**Fig. 1c, Supplementary Fig. 5d,e**), consistent with the pull-down assays (**Supplementary Fig. 2b,c**). Thus, by selectively stabilizing alternative conformational states of ASCT2, these findings demonstrate that S1-RBD binding is strongly dependent on the conformational state of ASCT2 and requires an outward-facing conformation, establishing a direct relationship between transporter conformation and receptor engagement.

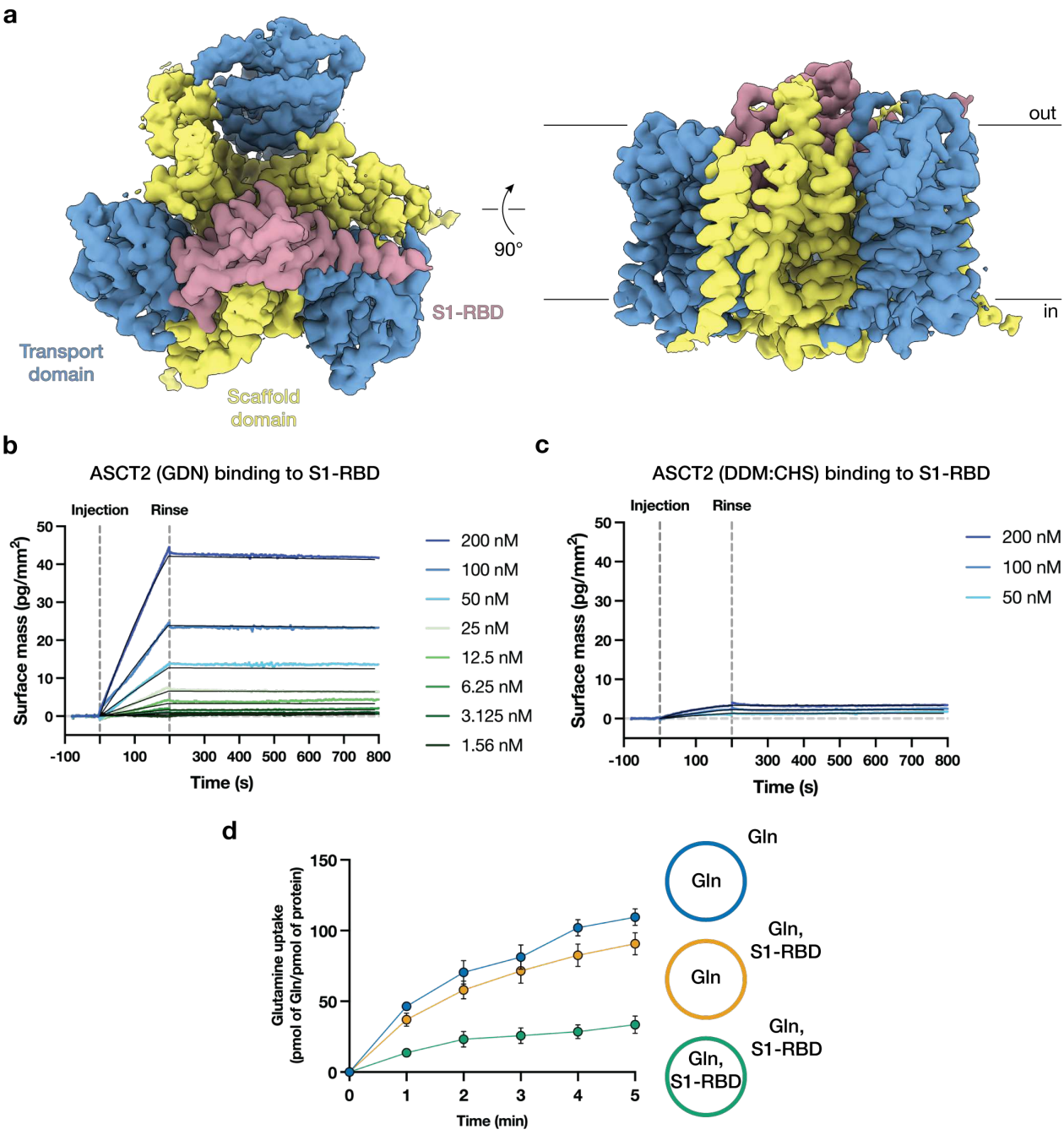


Figure 1 | S1-RBD binds to outward-facing ASCT2 with high affinity and reduces amino acid transport activity. a, Cryo-EM density map of Syncytin-1 receptor binding domain (S1-RBD, in pink) in complex with ASCT2 (transport domains in blue, scaffold domains in blue) purified in GDN detergent, viewed from the extracellular side (left) and from within the lipid bilayer (right). Membrane boundaries are shown as lines. **b-c,** Binding of ASCT2 solubilized in GDN (**b**) or DDM:CHS (**c**) detergents at increasing concentrations to S1-RBD, measured by GCI. The injection point indicates the start of ASCT2 injection; the rinse point marks the onset of surface rinsing with buffer. **d,** Glutamine transport mediated by Venus-tagged ASCT2 measured in the presence and absence of S1-RBD. Blue circle indicates ASCT2-reconstituted liposomes, yellow circle indicates ASCT2-reconstituted liposomes with externally added S1-RBD, and green circle indicates ASCT2-reconstituted liposomes with S1-RBD present on both sides of the liposomes. Data points represent mean values ± SD from two biological experiments, performed in two technical replicates.

Syncytin-1 engagement inhibits but does not abolish ASCT2 transport activity

The strict dependence of S1-RBD binding on outward-facing conformations of ASCT2, together with the contrast between our symmetric outward-facing structure and the presence of one inward-facing protomer in the previously reported ASCT2-Syncytin-1 complex[21], raised the possibility that Syncytin-1 engagement may interfere with the transport cycle. We therefore examined the functional consequences of S1-RBD binding on ASCT2-mediated amino acid transport. To this end, we measured amino acid exchange using a proteoliposome-based counterflow assay, which detects the exchange of luminal unlabeled glutamine for externally applied radiolabeled substrate. The reconstitution of ASCT2 into proteoliposomes yields both right-side-out oriented proteins, in which the extracellular surface of ASCT2 is accessible from the bulk solution, and inside-out oriented molecules, in which the extracellular surface is exposed to the luminal side of the liposome. While proteins in both orientations support the exchange of amino acids across the membrane, S1-RBD can only bind to the right-side-out oriented ASCT2 molecules when it was experimentally added. Addition of S1-RBD to the external side of liposomes resulted in a modest reduction in glutamine uptake compared with ASCT2 alone (**Fig. 1d**). Next, we tested whether the inclusion of S1-RBD inside the liposomes would further decrease transport activity. Liposomes were preloaded with S1-RBD, and an equal concentration of S1-RBD was added externally to ensure full saturation on both sides. Under these conditions, glutamine uptake decreased by approximately two-thirds (**Fig. 1d**). Thus, Syncytin-1 binding inhibits but does not completely abolish the ASCT2-mediated amino acid transport.

Because S1-RBD binds specifically to the extracellular face of ASCT2, we hypothesized that the small reduction in transport activity observed upon addition of S1-RBD on the external side of the liposomes might be a consequence of a preferred orientation adopted by ASCT2 in our proteoliposomes. In this case, a predominant inside-out orientation with the extracellular side facing the liposome lumen, making it unreachable for the added S1-RBD. To test this idea, we took advantage of the Venus fluorescent protein fused to the cytoplasmic side of ASCT2 and assessed protein orientation by proteolytic cleavage with 3C protease (**Supplementary Fig. 6a,b**). Application of 3C protease to the external side of the liposomes reduced the Venus signal by 60% compared to the untreated control, indicating that this fraction of ASCT2 molecules exposed their cytoplasmic side to the external solution. When protease was added to both the internal and external sides of the lipid vesicles, SDS-PAGE analysis showed a further 20% decrease in Venus fluorescence. The remaining ~20% signal likely corresponds to protease-inaccessible protein populations – possibly due to multilamellar vesicles – or incomplete cleavage due to protease inactivation. Assuming that this remaining fraction is either not active in transport (because present in internal membranes of multilamellar structures), or has the same proportion of right-side-out and inside-out proteins as the untreated liposomes (in case of incomplete protease activity), this data indicates that approximately 75% of ASCT2 molecules were oriented “inside-out,” with the cytoplasmic side exposed externally (**Supplementary Fig. 6b**). This orientation explains the limited inhibitory effect of externally added S1-RBD, which does not interact with the cytoplasmic side of ASCT2, on transport activity. Considering the orientation bias of ASCT2 in the proteoliposomes, these findings indicate that ASCT2 retains residual transport activity while still engaging with the receptor-binding domain of Syncytin-1.

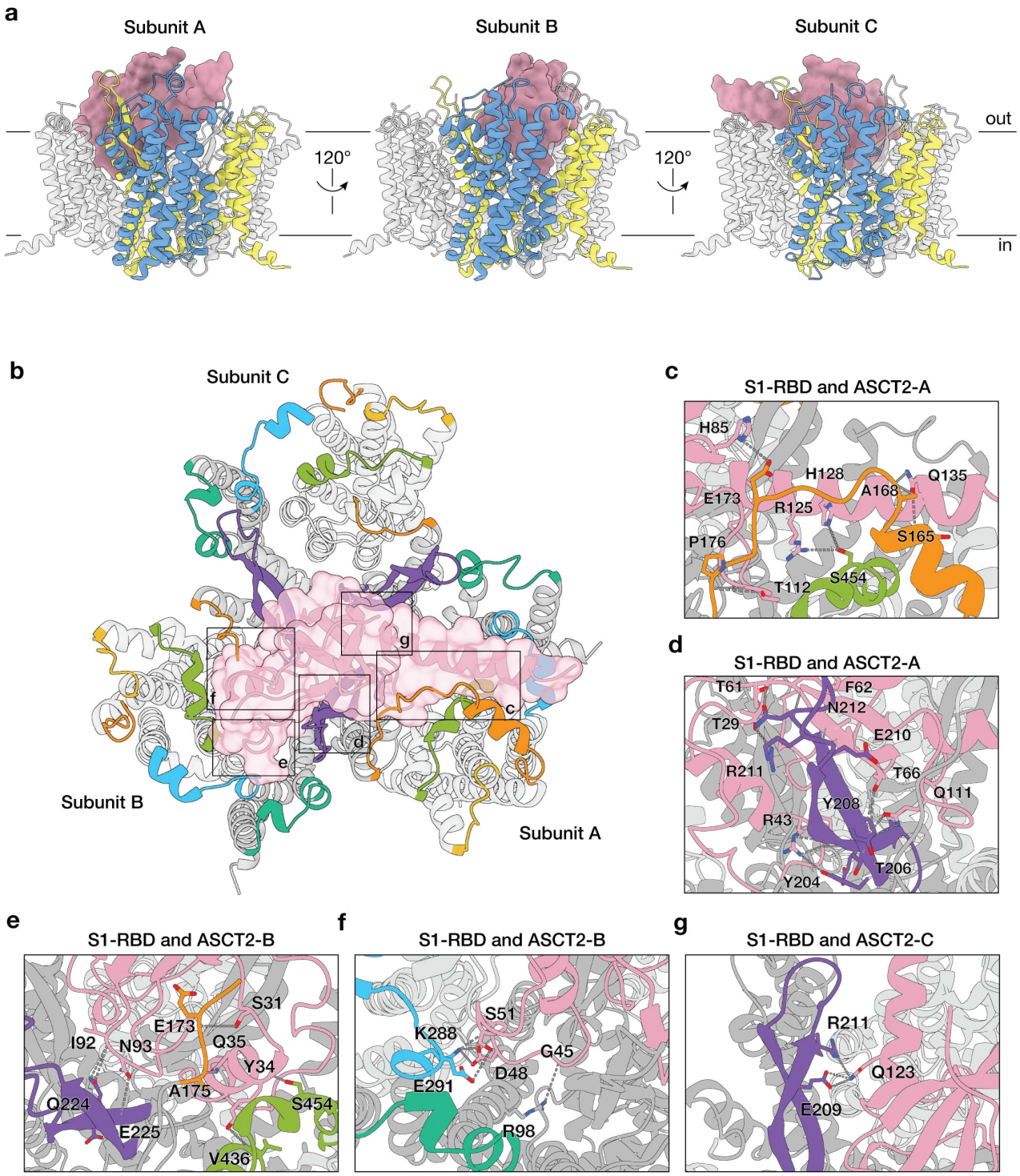


Figure 2 | S1-RBD binding interface on the ASCT2 trimer. a, Structure of the ASCT2-S1-RBD complex viewed from the membrane plane, highlighting the identical outward-facing position of the transport domains (blue) in each subunit. In each view, one protomer is colored by domains (scaffold domain in yellow, transport domain in blue), while the remaining two protomers are shown in gray. The S1-RBD is displayed as a pink surface. Membrane boundaries are shown as lines. **b,** Top view of the ASCT2 trimer bound to S1-RBD. Protomers are colored in gray. The S1-RBD is shown as a pink cartoon with transparent surface map. Extracellular loops are mapped on the trimer in distinct colors: ECL1 in teal, ECL2-C in orange, ECL2-N in purple, ECL3 in light blue, ECL4 in yellow, ECL5 in green. Insets correspond to interaction regions highlighted in panels **c-g**. **c-g,** Close-up views of S1-RBD interactions with ASCT2 regions: ECL2-C of subunit A (**c**), ECL2-N of subunit A (**d**), ECL2-N and ECL2-C of subunit B (**e**), ECL3 of subunit B (**f**), and ECL2-N of subunit C (**g**). Key interacting residues are shown as sticks. Gray dotted lines indicate molecular interactions.

S1-RBD forms an extensive, asymmetric binding interface with ASCT2

The observed conformation-specificity alongside the partial inhibition of transport activity raises the question of how Syncytin-1 engagement structurally constrains the receptor. To address this, we examined the molecular details of the ASCT2-S1-RBD interface revealed by our cryo-EM structure.

S1-RBD establishes a large and asymmetric binding interface with ASCT2, forming multiple contacts with individual protomers. These interactions are not identical, introducing unique structural asymmetries into the otherwise symmetric ASCT2 trimer. The binding interface primarily involves two ASCT2 protomers, referred to as subunits A and B, with the scaffold domains contributing most of the interaction interface (**Fig. 2a,b**).

Subunit A forms the most extensive contacts through two interaction sites. The first site involves the N-terminal region of the extracellular loop 2 (ECL2-N, corresponding to residues Gln154-Val180), which has been highly flexible in previous ASCT2 structures[19,25,26] but here it becomes ordered upon S1-RBD binding. At this site, the C-terminal part of S1-RBD interacts with the ASCT2 backbone through the side chain of $Gln135_{S1\text{-}RBD}$, which contacts the backbone of $Ser165_{ASCT2\text{-}A}$ and $Ala168_{ASCT2\text{-}A}$, while $Glu173_{ASCT2\text{-}A}$ forms contacts with the $His85_{S1\text{-}RBD}$ backbone (**Fig. 2c**). Additionally, hydrogen bonds between $Arg125_{S1\text{-}RBD}$ and $His128_{S1\text{-}RBD}$ and the hydroxyl group of $Ser454_{ASCT2\text{-}A}$ on TM8 stabilize the complex. During transport domain movement, leading to an inward-facing conformation, $Ser454_{ASCT2\text{-}A}$ shifts by approximately 22 Å across the membrane, accompanied by substantial displacement of ECL2-N. These displacements of contact sites might explain the lack of interaction of S1-RBD with the three-fold inward-facing ASCT2 when solubilized in DDM:CHS.

The second interaction site on subunit A involves the C-terminal region of ECL2 (ECL2-C, corresponding to residues Arg202-Asn230), which forms a β-strand with variable sequence among SLC1 family members. This flexible region is stabilized by a parallel β-strand from S1-RBD through an extensive network of hydrogen bonds, primarily involving backbone interactions from $Thr206_{ASCT2\text{-}A}$, $Tyr208_{ASCT2\text{-}A}$, and $Glu210_{ASCT2\text{-}A}$, and further supported by side-chain contacts from $Tyr204_{ASCT2\text{-}A}$, $Arg211_{ASCT2\text{-}A}$, and $Asn212_{ASCT2\text{-}A}$ (**Fig. 2d**).

Subunit B contributes fewer contacts to the interface. Its ECL2-C β-strand interacts with S1-RBD, particularly the side chain of $Gln224_{ASCT2\text{-}B}$, stabilizing the $Ile92_{S1\text{-}RBD}$ backbone (**Fig. 2e**). $Lys288_{ASCT2\text{-}B}$ of ECL3 forms multiple hydrogen bonds with the side chain of $Asp48_{S1\text{-}RBD}$ and the backbone oxygen of $Ala49_{S1\text{-}RBD}$, while $Arg98_{ASCT2\text{-}B}$ forms a hydrogen bond with $Gly45_{S1\text{-}RBD}$ (**Fig. 2f**). An additional interaction involves $Glu291_{ASCT2\text{-}B}$, which contacts $Ser51_{S1\text{-}RBD}$. $Glu291_{ASCT2\text{-}B}$, together with the nearby $Glu293_{ASCT2\text{-}B}$ residue in ECL3, undergoes a slight shift during transport domain movement, towards an inward-facing state, suggesting that recognition of these residues contributes to selective S1-RBD binding to the outward-facing state of the receptor.

In contrast, subunit C forms only limited contacts with S1-RBD. Hydrogen bonds are observed only between residues in the ECL2-C β-strand, including $Glu209_{ASCT2\text{-}C}$ and $Arg211_{ASCT2\text{-}C}$, and the side chain of $Gln123_{S1\text{-}RBD}$, supporting a key role for the C-terminal region of ECL2 in stabilizing S1-RBD on the ASCT2 trimer (**Fig. 2g**). Notably, unlike subunits A and B, S1-RBD interacts exclusively with the scaffold domain of subunit C and does not contact its transport domain. This arrangement suggests that the transport domain of this protomer may be capable of the elevator-like movements required for amino acid translocation while S1-RBD

remains bound. Consistent with this interpretation, ASCT2 retains measurable residual transport activity in the presence of S1-RBD (**Fig. 1d**).

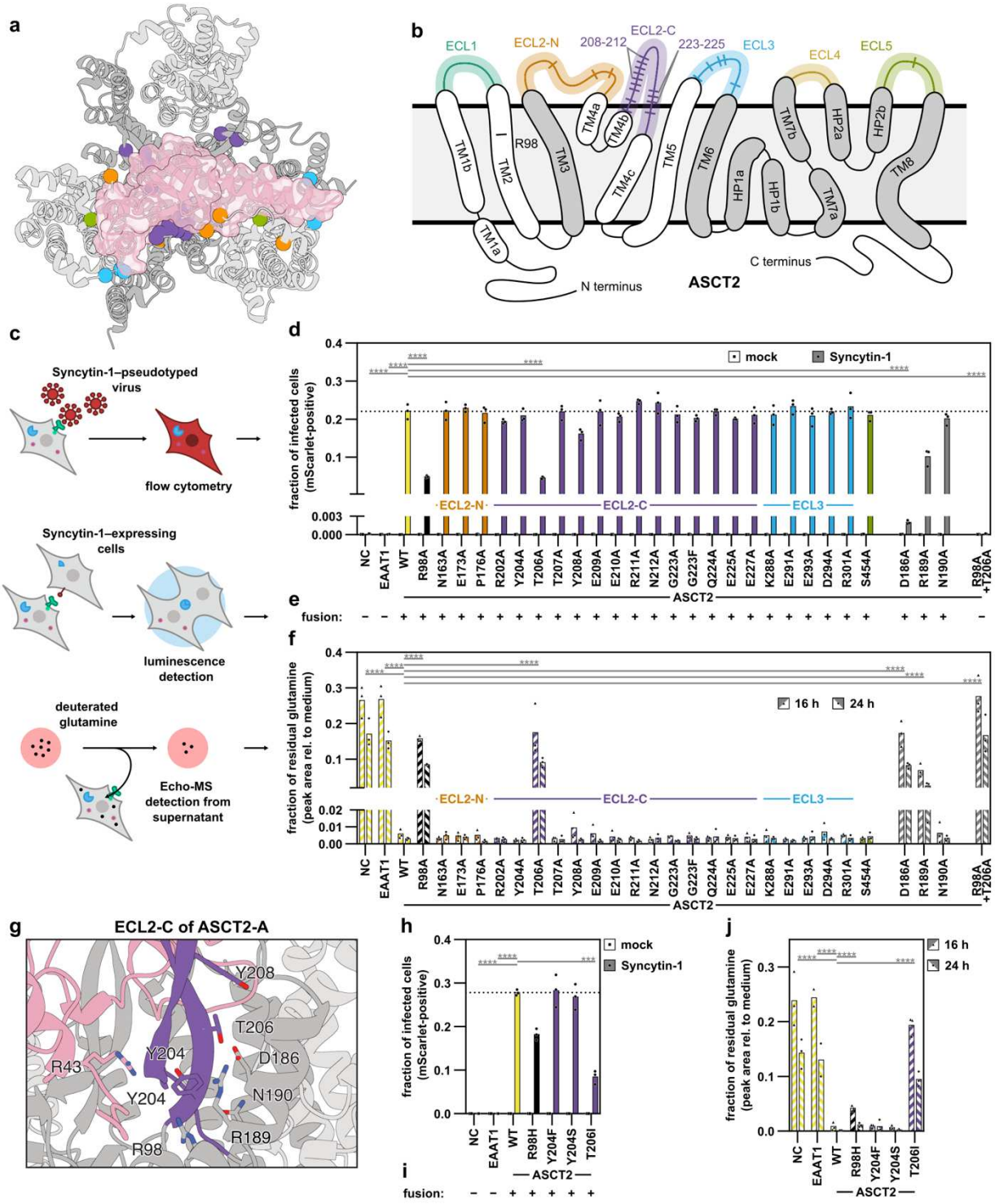


Figure 3 | Cell-based analysis of the interaction of ASCT2 alanine mutants with Syncytin-1. a, Structure of the ASCT2 trimer highlighting residues selected for alanine mutagenesis. Transport domains are shown in dark gray and the scaffold domain in light gray. Cα atoms of selected residues are depicted as spheres, colored by the extracellular loop. The S1-RBD is displayed as a pink cartoon with a transparent surface. **b,** Membrane topology of ASCT2 highlighting loop architecture. Substituted residues are marked by dashes colored according to their respective loops. **c,** Overview of the infection, fusion, and glutamine uptake assays performed in ASCT2-expressing cells. **d,** Infection efficiency of cells expressing individual ASCT2 mutants by Syncytin-1-pseudotyped virus. **e,** Fusion activity scored as + (detectable fusion) or – (no detectable fusion)

according to criteria described in the Methods section. **f**, Glutamine uptake by cells expressing individual ASCT2 mutants, shown as the fraction of residual glutamine remaining in the culture medium after 16 h or 24 h of cultivation. **g,** Close-up view of residues Arg98 and Thr206, whose substitution reduced infection sensitivity. Key interacting residues are shown as sticks; ASCT2 is colored gray, ECL2-C in purple, and S1-RBD in pink. **h,** Relative infection efficiency of cells expressing naturally occurring ASCT2 polymorphisms at Arg98, Tyr204, or Thr206 infected with Syncytin-1–pseudotyped virus. **i,** Receptor capacity of the selected polymorphisms in fusion assay. **j,** Glutamine uptake by cells expressing naturally occurring ASCT2 mutants, measured as the fraction of residual glutamine remaining in the culture medium after 16 h or 24 h. For panels **d**, **f**, **h**, **j**, NC, ASCT2/ASCT1 double-knockout HEK293T cells; EAAT1, double-knockout cells expressing EAAT1 (negative control); WT, double-knockout cells expressing wild-type ASCT2. For panels **d**, **f**, **h**, **j**, experiments were performed in biological triplicate; individual values and their means are shown. Statistical analysis was performed using repeated-measures two-way ANOVA with Dunnett's post hoc test versus WT on transformed data. Significance is indicated as ***, $P<0.001$; ****, $P<0.0001$; P-values > 0.05 not shown.

Single-residue substitutions in ASCT2 reduce Syncytin-1 recognition and glutamine uptake

To systematically define the contributions of individual residues to receptor recognition, we designed a panel of ASCT2 mutants carrying alanine substitutions across extracellular regions spanning the binding interface (**Fig. 3a,b**). All variants were stably ectopically expressed in HEK293T cells lacking endogenous expression of ASCT2 and ASCT1, and their expression levels and plasma membrane localization were verified (**Supplementary Figs. 7, 8**). We then assessed the functional impact of these mutations on interaction with Syncytin-1 using three complementary assays: binding of S1-RBD to living cells expressing the ASCT2 variants; infection of cells with non-replicative Syncytin-1-pseudotyped virus; and Syncytin-1-mediated cell-cell fusion (**Fig. 3c, Supplementary Fig. 9a,b**). Among these, the pseudovirus infection assay exhibited the highest dynamic range in sensitivity and reports both receptor engagement and physiologically relevant steps leading to membrane fusion.

Most single substitutions displayed infection levels comparable to wild-type ASCT2, suggesting that individual substitutions are not sufficient to disrupt Syncytin-1 recognition (**Fig. 3d**). This tolerance is consistent with the extensive interaction interface observed in the cryo-EM structure. Across all three assays, S1-RBD binding to ASCT2 variants on living cells closely mirrored the infection results (**Supplementary Fig. 9c**), while the cell–cell fusion assay showed greater substitution tolerance, with no single mutant abolishing Syncytin-1-mediated fusion (**Fig. 3e, Supplementary Fig. 10**). Notably, two single mutations – R98A and T206A – significantly reduced susceptibility to Syncytin-1-mediated infection and decreased S1-RBD binding, identifying these residues as critical for Syncytin-1 engagement (**Fig. 3d, Supplementary Fig. 9**).

Structurally, $Arg98_{ASCT2\text{-}B}$, located in the middle of TM2 within the scaffold domain, forms a hydrogen bond with $Gly45_{S1\text{-}RBD}$ and participates in π-cation interactions with $Tyr204_{ASCT2\text{-}A}$, which resides on the extracellular β-strand of ECL2-C and coordinates $Arg43_{S1\text{-}RBD}$ (**Fig. 3g**). Similarly, $Thr206_{ASCT2\text{-}A}$, positioned near $Tyr204_{ASCT2\text{-}A}$, is part of an interaction network involving $Asp186_{ASCT2\text{-}A}$ and $Arg189_{ASCT2\text{-}A}$, located on TM4a. This network is structurally connected to $Arg98_{ASCT2\text{-}B}$, linking the extracellular loop and transmembrane region of the binding interface. Consistently, alanine substitutions at $Asp186_{ASCT2\text{-}A}$ and $Arg189_{ASCT2\text{-}A}$ also reduced Syncytin-1-mediated infection and decreased S1-RBD binding (**Fig. 3d, Supplementary Fig. 9c**), although these mutants retained fusion capacity (**Fig. 3e, Supplementary Fig. 10**). All single-residue ASCT2 variants, including R98A, T206A, D186A, and R189A, showed comparable expression and plasma membrane localization, indicating that functional differences do not arise from cellular trafficking defects

(**Supplementary Fig. 7, 8**). To assess whether these mutations affect transporter function, we measured cellular glutamine and serine uptake. Cells expressing wild-type ASCT2 and most single mutants depleted deuterated amino acids from the medium within 24 hours. In contrast, R98A, T206A, D186A, and R189A mutants consistently showed impaired glutamine uptake (**Fig. 3f, Supplementary Fig. 11**). It is noteworthy that mutations that reduce Syncytin-1 engagement also compromise ASCT2 transport activity.

Finally, we generated a double mutant combining R98A and T206A. In contrast to the partial effects observed for single substitutions, this combined mutant completely abolished interaction with Syncytin-1 in all three assays, demonstrating that additive contributions from multiple interface residues are required for effective receptor recognition (**Fig. 3d,e, Supplementary Fig. 9c**).

Additionally, we examined rare human polymorphisms affecting these residues, including R98H, Y204F, Y204S, and T206I, to assess the physiological relevance of these findings. None of these variants impaired cell–cell fusion, consistent with the overall tolerance of the fusion assay to partial reductions in receptor engagement (**Fig. 3i, Supplementary Fig. 10**). However, similar to the alanine substitutions, R98H and T206I reduced S1-RBD binding and Syncytin-1-pseudovirus infection and showed reduced amino acid uptake (**Fig. 3h,j, Supplementary Fig. 9c, 11**).

Together, these data establish the biological relevance of the extensive cryo-EM–defined interface and demonstrate that Syncytin-1 recognition depends on the integrity of the interaction surface rather than on single residues. Notably, receptor function is preserved in variants that retain amino acid transport activity.

Extensive ECL2-C substitution in ASCT2 reduces Syncytin-1 recognition

To further define the contribution of extracellular loops, we generated ASCT2 variants containing multiple alanine substitutions across individual ECLs and assessed their interaction with Syncytin-1 in cell-based assays (**Fig. 3b, Supplementary Table 2**). Shortening the ECL1 loop, substituting residues in ECL2-N, or mutating ECL3 did not affect infection by Syncytin-1-pseudotyped virus (**Fig. 4a**). Combined mutations within ECL1 and ECL3 also showed no effect (**Fig. 4a**). In contrast, substitutions in ECL2-C, either alone or in combination with ECL2-N substitutions, resulted in loss of detectable receptor protein expression (**Fig. 4d, Supplementary Figs 8,9**). To improve protein stability, we subdivided the ECL2-C mutant into two variants targeting residues 208-212 and 223-225 separately (**Fig. 3b**). The 223-225 mutant was well expressed and remained sensitive to Syncytin-1-pseudotyped virus. In contrast, substitution of residues 208-212 conferred complete resistance to infection while preserving expression levels (**Fig. 4a,d, Supplementary Figs. 7,8**). The S1-RBD binding assay showed reduced binding for all extensive ECL substitutions except ECL2-N (**Supplementary Fig. 9c**). In contrast, cell-cell fusion was not affected in well-expressed mutants (**Fig. 4b, Supplementary Fig. 10**). Glutamine uptake assay mirrored Syncytin-1-pseudovirus infection results, showing that mutants with impaired interaction with Syncytin-1 have also affected transport function (**Fig. 4c, Supplementary Fig. 11**). In addition, glutamine uptake was also reduced in the ECL3 mutant containing four alanine substitutions (**Fig. 4c**). Together, these results identify residues 208-212 in the C-terminal region of ECL2 as essential for Syncytin-1 engagement and for transporter function. Structurally, this region contacts S1-RBD in all three ASCT2 protomers, which explains the pronounced functional defect. These findings define specific extracellular residues and regions that are required for Syncytin-1 recognition of ASCT2.

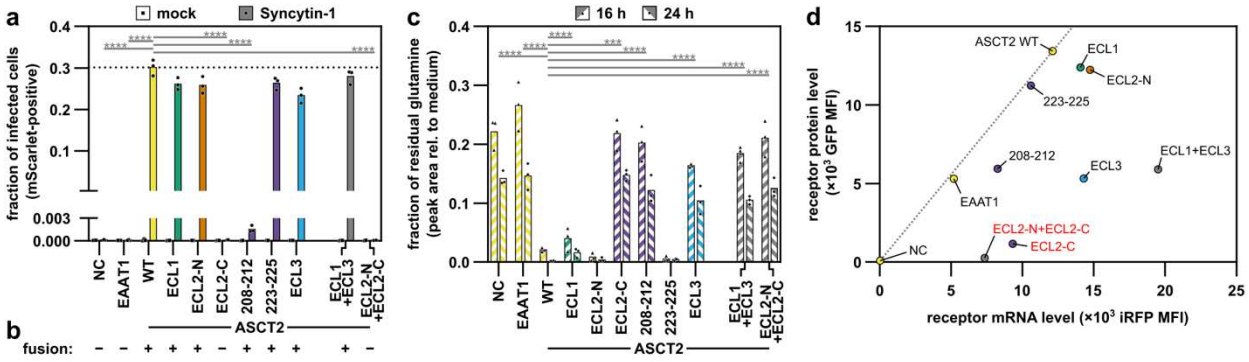


Figure 4 | Interaction of ASCT2 extracellular loop mutants with Syncytin-1. a, Sensitivity of cells expressing ASCT2 ECL mutants to Syncytin-1-pseudotyped virus. **b,** Fusion activity scored as + (detectable fusion) or – (no detectable fusion), as defined in Methods. **c,** Glutamine uptake in cells expressing individual ASCT2 mutants, measured as the fraction of residual glutamine remaining in the culture medium after 16 h or 24 h of cultivation. **d,** Expression analysis of ASCT2 extracellular loop mutants, comparing mRNA levels (median fluorescence intensity of iRFP, *x*-axis) and protein expression (median fluorescence intensity of GFP, *y*-axis). Average values of three independent measurements are shown with poorly expressed mutants highlighted in red. The dotted line connecting NC and ASCT2 WT shows the expected ratio of protein and mRNA levels. NC, ASCT2/ASCT1 double-knockout HEK293T cells; EAAT1, double-knockout cells expressing EAAT1 (negative control); WT, double-knockout cells expressing wild-type ASCT2. For panels **a, c**, experiments were performed in biological triplicate, with individual values and their means shown. Repeated-measures two-way ANOVA with Dunnett's post hoc test versus WT was performed on transformed data and P-values are shown as follows: ***, P<0.001; ****, P<0.0001. P-values higher than 0.05 are not shown.

Gain-of-function mutations in ASCT1 increase Syncytin-1 recognition

Although the ASCT2 mutants R98A and T206A show reduced interaction with Syncytin-1, the corresponding wild-type residues Arg98 and Thr206 are conserved in ASCT1 (**Supplementary Fig. 12**), an SLC1 family member that does not function as a Syncytin-1 receptor[23]. Despite the high sequence and structural similarity between ASCT1 and ASCT2, only ASCT2 supports Syncytin-1 recognition, suggesting that the identified residues are necessary but not sufficient for receptor function. In contrast, residues within ECL2-N and ECL2-C differ between ASCT1 and ASCT2, indicating that these regions may contribute to receptor specificity. To define the molecular basis of receptor specificity, we generated gain-of-function ASCT1 variants in which extracellular residues forming the Syncytin-1 binding interface were replaced with their ASCT2 counterparts and tested their interaction with Syncytin-1 (**Fig. 5a, Supplementary Tab. 3**).

Substitution of residues in ECL1 resulted in a small but significant increase in sensitivity to Syncytin-1-mediated infection and fusion activity (**Fig. 5b,c**). Exchange of four residues in ECL3 also enhanced Syncytin-1 recognition, largely due to the single substitution K285E (**Fig. 5b,c**). In contrast, reciprocal mutation in ASCT2 (E293K or E291K) did not reduce infection or fusion (**Fig. 5d,e**), consistent with an extensive interaction interface that tolerates single residue changes.

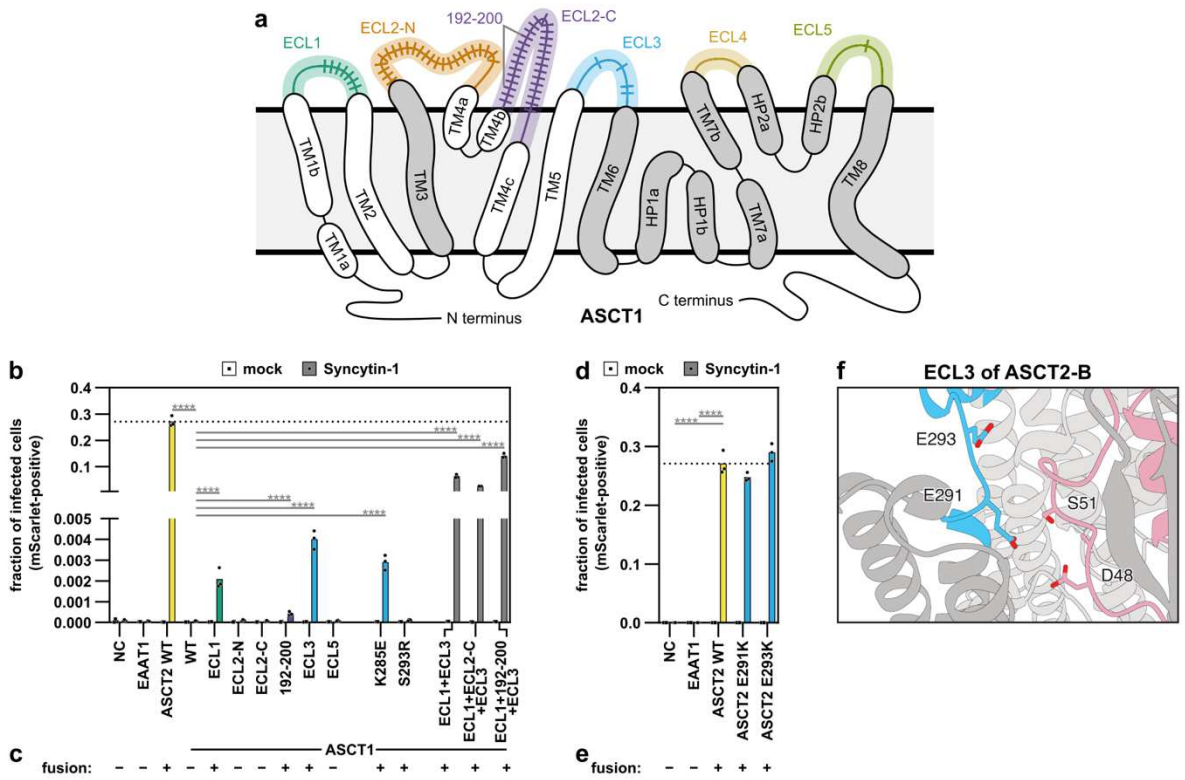


Figure 5 | Interaction of gain-of-function ASCT1 mutants with Syncytin-1. a, Schematic representation of ASCT1 loop architecture. Residues substituted with their ASCT2 counterparts are indicated by dashes and colored according to their respective loops. Transport domains are shown in gray and scaffold domain in white. **b,** Relative infection of cells expressing ASCT1 chimeric constructs by Syncytin-1-pseudotyped virus. **c,** Fusion activity indicated by + (detectable fusion) or – (no detectable fusion) as defined in Methods. **d,** Relative infection of cells expressing ASCT2 constructs carrying reciprocal E291K or E293K substitutions by Syncytin-1-pseudotyped virus. **e,** Fusion activity indicated by + (detectable fusion) or – (no detectable fusion). **f,** Close-up view of ASCT2 residue E293, which contributes to increased Syncytin-1 sensitivity observed with ASCT1 K285E mutant in the infection assay. NC, ASCT2/ASCT1 double-knockout HEK293T cells; EAAT1, double-knockout cells expressing EAAT1 (negative control); WT, double-knockout cells expressing either wild-type ASCT1 or wild-type ASCT2. For panels **b** and **d**, experiments were performed in biological triplicate. Individual values with their means are shown. Repeated-measures two-way ANOVA with Dunnett's post hoc test versus ASCT1 WT or ASCT2 WT was performed on transformed data and P-values are shown as follows: ****, P<0.0001. P-values higher than 0.05 are not shown.

We also assessed the contribution of other extracellular loops. The substitution of ECL2-N or ECL5 in ASCT1 did not confer a gain of function. Similarly, substitution of the ASCT1 ECL-C region (residues 190-218) with ASCT2 residues 203-226 also did not influence Syncytin-1 recognition. Although this region was suggested as a key determinant of Syncytin-1 binding, the protruding β-strand is present in both ASCT1 and ASCT2, and its exchange is not sufficient to generate a functional Syncytin-1 binding interface.

Guided by the ASCT2 208-212 mutant results (**Fig. 4a**), which conferred complete resistance to Syncytin-1 binding, we replaced ASCT1 residues 192-200 with corresponding ASCT2 residues 205-213. This substitution produced a modest increase in sensitivity to Syncytin-1-pseudotyped virus infection and fusion (**Fig. 5b,c**), suggesting that Syncytin-1 recognition depends on specific residues rather than on receptor secondary structure alone.

Finally, we tested the collective contribution of multiple extracellular loops to Syncytin-1 recognition. Incorporation of both ECL1 and ECL3 from ASCT2 into ASCT1 markedly increased the infection sensitivity to approximately 30% of wild-type ASCT2 levels (**Fig. 5b**). Addition of the 192-200 substitution in ECL2-C further increased sensitivity to Syncytin-1-enveloped virus to around 50% of wild-type ASCT2 and enabled detection of S1-RBD binding (**Fig. 5b, Supplementary Fig. 9c**). In agreement, all combined extracellular loop substitutions conferred cell-cell fusion competence of the ASCT1 gain-of-function mutants (**Fig. 5c, Supplementary Fig. 10**). Importantly, all ASCT1 chimeras were correctly localized and retained the substrate selectivity, with preference of serine transport rather than glutamine, indicating that these substitutions do not alter intrinsic transport specificity (**Supplementary Figs. 7, 11**).

Together, these gain-of-function analyses demonstrate that multiple extracellular ASCT2 regions likely cooperate to form the Syncytin-1 recognition site and that receptor specificity arises from coordinated contributions across domains rather than from individual residues alone.

Discussion

Syncytin-1 drives human placental development by binding the Na^+-dependent neutral amino acid transporter ASCT2 and inducing membrane fusion[27]. This interaction forms the multinucleated syncytial layer essential for nutrient exchange between mother and fetus. In this study, we dissect the molecular basis of the ASCT2-Syncytin-1 interaction, providing the following key insights: (1) Syncytin-1 recognition requires the outward-facing conformation of ASCT2; (2) binding occurs with high affinity and slow dissociation; (3) receptor engagement reduces, but does not abolish, ASCT2-mediated amino acid transport, (4) recognition is governed by the overall architecture of an asymmetric interface, (5) and shaped by contributions from multiple residues and molecular differences between ASCT2 and ASCT1; (6) receptor competence correlates with preserved transporter function.

Our data demonstrate that Syncytin-1 binding is tightly coupled to the conformational state of ASCT2. When ASCT2 was extracted from the plasma membrane using DDM supplemented with CHS – a membrane-mimicking environment known to stabilize the inward-facing state[19,25] – complex formation was inefficient, indicating that this conformation is incompatible with Syncytin-1 recognition. In contrast, solubilization in GDN, a detergent that favors the outward-facing state, enabled the robust complex formation and cryo-EM structure determination. Binding measurements corroborated this dependence: ASCT2 purified in GDN showed strong binding to Syncytin-1, whereas DDM:CHS-solubilized protein showed markedly reduced binding. Interestingly, kinetic analysis of DDM:CHS-solubilized ASCT2 also yielded bona fide binding curves (**Fig. 1c**), although the binding responses were substantially reduced in intensity. This suggests that a minor fraction of ASCT2 molecules remains compatible with S1-RBD binding, likely due to transient sampling of the outward-facing state. However, this fraction was insufficient for detection in the biochemical pull-down assay (**Supplementary Fig. 2b**), and conversion of ASCT2 from the binding-incompetent to binding-competent state is apparently slow relative to the duration of the assay.

The binding affinity measurements revealed a tight interaction between S1-RBD and ASCT2 with a dissociation constant K_D in the low nanomolar range, comparable with the kinetics observed for Friend Murine Leukemia Virus (FrMLV) and the Cationic Amino acid Transporter 1 (CAT1)[28]. An exact K_D value could not be determined as we could not detect sufficient dissociation within the timeframe of 10 minutes, consistent with

slow off-rates. Such a high affinity contrasts sharply with a previously reported value of ~1 μM affinity[21]. The previous estimate was derived from indirect GFP fluorescence measurements using GFP-tagged ASCT2 binding to immobilized Syncytin-1, which lacks the accuracy of direct kinetic measurements. In addition, the prior study used a consensus ASCT2 construct in which 10% of residues were replaced with frequently occurring vertebrate SLC1 variants to enhance protein stability[29]. In our infection assay, this consensus construct demonstrated markedly reduced interaction with Syncytin-1, indicating that these substitutions compromise receptor function (**Supplementary Fig. 13**). Furthermore, ASCT2 in the previous study was purified in DDS detergent, which is structurally similar to the DDM molecule and likely favors the inward-facing conformation, thereby potentially shifting the conformational equilibrium toward a binding-incompetent state. Taken together, differences in construct design, assay format, and detergent conditions provide a plausible explanation for the discrepancy in reported affinities. Our use of purified wild-type ASCT2 combined with direct kinetic measurements by GCI provides a more accurate assessment of the high-affinity interaction between ASCT2 and Syncytin-1.

The Syncytin-1 binding interface is extensive and asymmetric, spanning the ASCT2 trimer. While all three scaffold domains contribute to Syncytin-1 engagement, only two transport domains participate directly in binding, leaving the third protomer largely unengaged. In our structure, all three protomers adopt the outward-facing conformation, whereas a previous structure reported an asymmetric conformation with one protomer residing in an inward-facing state[21]. The absence of direct contacts with the third transport domain suggests that this protomer may retain the conformational flexibility required for amino acid exchange. Consistent with this interpretation, functional assays demonstrate that ASCT2 retains residual transport activity in the presence of Syncytin-1. This activity is likely mediated by the unbound third protomer. Therefore, Syncytin-1 binding does not completely abolish ASCT2 transport function, indicating that the transporter can contribute to amino acid homeostasis in syncytiotrophoblast cells while simultaneously participating in membrane fusion.

Structurally, a single S1-RBD engages the central extracellular cavity of the ASCT2 trimer, oriented parallel to the membrane plane. Since full-length Syncytin-1 is a homotrimer with each protomer containing an RBD, we cannot exclude the possibility that additional RBDs engage with the same ASCT2 trimer. However, the central cavity can accommodate only one RBD, making simultaneous binding at this site sterically impossible. Instead, each Syncytin-1 RBD may interact with a separate ASCT2 trimer, raising the possibility that clustering of multiple ASCT2 trimers is required to trigger membrane fusion. Whether such higher-order assemblies are required, and how membrane curvature and local bending coordinates this process, remains an important question for future studies using the full-length complex in a lipid bilayer environment.

At the molecular level, the S1-RBD engages through numerous asymmetric contacts across individual ASCT2 protomers, consistent with the binding interface described previously[21]. The most prominent interaction involves the C-terminal portion of ECL2 (ECL2-C), which forms an extracellular β-sheet previously proposed as a retroviral docking site[20]. Our findings confirm that this region contributes to receptor engagement but also demonstrate that is not sufficient on its own to determine Syncytin-1 recognition. In addition to contacts within ECL2-C, S1-RBD interacts with ECL1 and ECL3, indicating that receptor binding is distributed across multiple extracellular elements.

Beyond its role in receptor recognition, the ECL2-C β-sheet has been implicated in ASCT2 trafficking to the plasma membrane[30,31]. Consistent with these reports, extensive alanine substitutions within ECL2-C affected surface expression, confirming its structural importance for protein stability and proper localization (**Supplementary Fig. 7**). In addition, N-linked glycosylation sites are located within ECL2, at Asn163 (ECL2-N) and at Asn212 (ECL2-C)[32], and have been proposed to contribute to envelope glycoprotein binding[14,20]. However, more recent evidence suggests that glycosylation is not required for Syncytin-1 recognition[30]. Consistent with this notion, single-site mutations eliminating glycosylation did not affect Syncytin-1 infection in our assays (**Fig. 3d, Supplementary Fig. 13**). Simultaneous substitution of both sites resulted in only a modest reduction in interaction, most likely reflecting decreased surface expression rather than impaired receptor recognition (**Supplementary Fig. 13**).

Alanine screening of residues directly contacting S1-RBD revealed that most single substitutions did not affect Syncytin-1 recognition in infection assays. Only two mutations, R98A and T206A, substantially reduced - but did not eliminate - Syncytin-1-pseudotyped virus entry and S1-RBD binding, despite normal protein expression and plasma membrane localization (**Fig. 3d, Supplementary Fig. 7, 8b, 9c**). Both residues reside within the scaffold domain and are highly conserved across the SLC1 family. These residues likely participate in an interaction network that influences the positioning of the extracellular β-region and thereby modulates its compatibility with Syncytin-1 docking. Notably, the same mutants also exhibited reduced glutamine transport activity (**Fig. 3f**). This functional overlap does not imply a direct mechanistic link between Syncytin-1 binding and ASCT2 transport function. Rather, these substitutions could perturb the structural integrity or conformational equilibrium of ASCT2, thereby affecting both processes. Consistent with this interpretation, the scaffold domain is not directly involved in substrate translocation, suggesting that the observed transport reduction arises independently, potentially through shifts in conformational equilibria that also disfavor the state required for S1-RBD binding.

ASCT1 – the closest SLC1 family homolog – shares with ASCT2 the same overall trimeric architecture and contains similar extracellular β-strands in ECL2[22], yet it does not support Syncytin-1-mediated fusion[23]. Our findings shed light on the differences between the two proteins in Syncytin-1 receptor interaction. Introducing ASCT2-specific single-point substitutions or replacement of individual extracellular loops into ASCT1 is insufficient to confer efficient receptor competence. However, an ASCT1 variant harboring multiple substitutions across ECL1-3 restored substantial sensitivity to Syncytin-1-pseudotyped virus, reaching approximately half of the interaction level observed with wild-type ASCT2. These findings argue against a recognition mechanism driven by a small number of critical residues or by the conserved β-sheet architecture alone. Instead, they support a model in which Syncytin-1 engagement emerges from the cumulative contribution of multiple residues distributed across an extended extracellular interface within the trimeric transporter.

The robustness of this interaction is further highlighted by species-specific differences. Murine ASCT2, which is resistant to Syncytin-1-mediated infection, contains a 13-amino-acid insertion within the ECL2-C region[14,23]. Structural modeling suggests that this elongated ECL2-C segment bends towards the central cavity of the trimer, where it likely sterically hinders Syncytin-1 binding (**Supplementary Fig. 14**). To date, this insertion represents the only observed mechanism of ASCT2 resistance, further underscoring the

robustness of the Syncytin-1 and ASCT2 interaction. Indeed, the receptor surface engaged by Syncytin-1 is the most extensively described for glycoproteins of enveloped viruses (**Supplementary Tab. 4**), which likely contributes to both the high binding affinity and the pronounced tolerance to single-residue mutations.

Finally, the functional relevance of this extensive interface is reflected in our cell-based assays. Although the three assays converged on the same overarching conclusions, they differed in sensitivity and dynamic range, consistent with their distinct biological contexts. Infection with Syncytin-1–pseudotyped virus was the most sensitive and provided the broadest quantitative window, enabling discrimination of subtle differences in receptor competence. In contrast, cell-based S1-RBD binding assays displayed higher background and lower sensitivity, mirroring the kinetics of the binding. Nevertheless, they reproduced the relative trends observed in infection assays, supporting the notion that receptor engagement is the primary determinant of infectivity (**Supplementary Fig. 9)**. The cell–cell fusion assay was highly sensitive in detecting receptor function but yielded predominantly binary outcomes and tolerated substantial alterations within the interaction interface (**Supplementary Fig. 10)**. This suggests that the threshold for membrane merger is lower than that required for efficient viral entry. The difference likely reflects the distinct physical contexts of the processes: viral particles must engage the receptor efficiently within a limited time window while diffusing in the extracellular milieu, whereas during cell–cell fusion, both partners are membrane-anchored in two neighboring adherent cells and can establish repeated or stabilized contacts. In the physiological context of syncytiotrophoblast fusion, such sustained interactions may further favor higher tolerance of Syncytin-1 recognition against moderate alterations in the ASCT2 interface.

In conclusion, Syncytin-1 recognition depends on the precise spatial arrangement of an extensive extracellular interface rather than on individual contact residues. Accordingly, most single substitutions do not impair fusion competence. Notably, in the ASCT2 mutations that most strongly reduced the interaction with Syncytin-1, including rare human ASCT2 polymorphisms, glutamine transport was also compromised. Conversely, Syncytin-1 engagement with ASCT2 reduced but did not abolish its transport activity. Given the central role of glutamine transport to placental metabolism, partial preservation of transporter function during receptor engagement may have minimized the physiological cost associated with Syncytin-1 endogenization and exaptation. This functional compatibility would allow trophoblast fusion to proceed without fully compromising amino acid exchange, maintaining a subtle balance between membrane fusion and metabolic support. These observations further suggest that single-nucleotide polymorphisms in ASCT2 are unlikely to selectively impair trophoblast fusion without simultaneously compromising transport activity.

Methods

Cell lines

For protein expression, we used HEK293S GnTI- cells (ATCC CRL-3022) growing in suspension. The cells were cultured at 37°C, 5% CO2, 70% humidity by shaking at 185 r.p.m. in TPP600 bioreactors in HyClone HyCell TransFx-H transfection media (Cytiva) supplemented with 1% FBS, 0.1% poloxamer 188, 2 mM glutamine, and antibiotic-antimycotic solution. Sf9 cells (ThermoFisher Scientific, 12659017) were grown at 27°C and 130 r.p.m. in SFM-III medium supplemented with antibiotic–antimycotic solution. Cells were tested negative for mycoplasma contamination.

For Syncytin-1-pseudotyped viral infections, we used the ASCT1/2 CRISPR-Cas9-mediated double knockout clone FE-L that was derived from the HEK293T cell line as described before[23] and was grown in DMEM medium supplemented with 5% fetal calf serum, 5% calf serum, streptomycin (100 µg ml^{-1}), and penicillin (100 U ml^{-1}). Cells were cultured in a humidified incubator at 37°C in a 5% CO_2 atmosphere.

S1-RBD expression and purification

The S1-RBD construct was developed for receptor binding assay and reported recently[23]. Briefly, the receptor-binding domain of Syncytin-1 (S1-RBD) fused to TEV protease cleavage site and the constant region of the rabbit IgG gene was inserted into pLIB vector from the biGBac system[33]. Gene inserted into pLIB vector was confirmed via Sanger sequencing (Source Bioscience, Cambridge) before downstream steps.

The pLIB plasmid was transformed into chemically competent DH10 EMBacY E. coli cells (Geneva Biotech). Cells were then plated onto LB agar plates containing gentamycin, tetracycline, kanamycin, IPTG and X-gal and incubated at 37°C overnight. Colonies were picked via blue-white selection for overnight liquid culture and then, the bacmid DNA was isolated by alkali denaturation utilizing buffers P1, P2 and N3 from QIAprep Spin Miniprep Kit (QIAGEN), followed by isopropanol precipitation. Sf9 cells, grown in the Insect-XPRESS Insect Cell Culture Media with L-Glutamine (Lonza) supplemented with Penicillin-Streptomycin (Gibco), were transfected with recombinant bacmid using FuGENE HD Transfection Reagent (Promega) according to the manufacturer´s protocol and incubated at 28°C for 3-4 days. Supernatants of these cultures were used to generate baculovirus P1 stocks stored at 4°C, and these stocks were subsequently used to infect cultures of Sf9 cells for large-scale expression.

To express soluble S1-RBD, Sf9 cells were split to a cell density of 0.6×10^6 and the P1 viral stock was diluted 1:100 into the expression culture. Protein was expressed for 72h at 27°C to the supernatant. Cells were centrifuged at 1000×g for 10 min at RT, the supernatant was filtered through a 0.2 µm filter, and BioLock solution was added to block endogenous biotin. All subsequent purification steps were performed at 4°C. S1-RBD was purified using an XK 26/40 chromatography column (Cytiva) packed with Strep-TactinXT 4Flow resin (4 ml bed volume) equilibrated in wash buffer XT (100 mM Tris pH 8.0, 150 mM NaCl, 1 mM EDTA). The supernatant was passed through the column connected to an FPLC system overnight. Subsequently, the resin was washed with approximately 40 ml of wash buffer XT. S1-RBD was eluted with 20 ml total volume of elution buffer XT (100 mM Tris pH 8.0, 150 mM NaCl, 1 mM EDTA, 50 mM biotin), collecting 0.5 ml elution fractions. The protein concentration of all fractions was determined by measuring the absorbance at the 280nm channel on a nanodrop device. The elution fractions with the highest protein concentration were

concentrated using a 10-kDa MWCO Amicon Ultra concentrator to at least 0.3 mg ml^{-1}, flash frozen in LN2, and stored at -80°C until further use.

ASCT2 expression

The gene encoding ASCT2 (SLC1A5, Uniprot ID Q15758) was synthesized by GenScript and inserted into the expression vector pEZT-BM (a kind gift from Ryan Hibbs; Addgene plasmid no. 74099)[34], adapted for FX cloning[35] with a C-terminal HRV-3C cleavage site, followed by Venus, myc- and SBP-tags. Protein was expressed following the BacMam expression method[36]. Bacmid was prepared according to the Bac-to-Bac protocol (Invitrogen). Next, the virus was prepared according to the published protocol[34]. Briefly, Sf9 cells were seeded to at 1×10^6 cells per well in a six-well plate and transfected with bacmid using the Cellfectin II reagent (ThermoFisher Scientific). After 5 days of transfection, the supernatant containing the P0 virus was harvested and filtered. To generate the P1 virus, Sf9 cells were split into 1×10^6 cells in suspension and infected with the P0 virus (diluted at 1:1000). When approximately 80% of Sf9 cells were GFP fluorescent (after 3-4 days), the supernatant was harvested, filtered using 0.4 µm pore filter, supplemented with 10% FBS, and stored at 4°C in dark until further use. For large-scale expression, HEK293S cells were diluted to a cell density of 0.6×10^6. After 24h of incubation, the P1 viral stock was added at 1:1000 dilution, and the cells were cultured at 37°C for another 24h. Afterwards, the cells were supplemented with sodium butyrate at a final concentration of 10 mM, and protein was expressed at 30°C for 48h. Cells were harvested by centrifugation at 550×g, washed with 1×PBS, and stored at −80 °C until further use.

ASCT2 purification

All purification steps were performed at 4°C. Cell pellet, corresponding to roughly 200 ml cell culture, was usually used for a single purification. First, ASCT2 was solubilized in buffer A (20 mM Tris pH 7.4, 300 mM NaCl, 10% glycerol, 3 mM $MgCl_2$, 0.1 mg ml^{-1} DNase I, complete protease inhibitor tablets, 1% DDM:CHS (10:1), 1 mM glutamine) for 1h while rotating. Next, the insoluble cell fraction was removed by ultracentrifugation at 442,907×g for 30 min. Subsequently, various affinity purifications and detergent choices were employed depending on the downstream biochemical analysis.

To purify tagless ASCT2, NHS-activated Sepharose with immobilized 3K1K nanobody (3K1K resin) was used to capture the Venus tag on ASCT2. The supernatant with solubilized ASCT2 was incubated with the 3K1K resin in batch for 1h. Afterward, the unbound protein was removed in a flow-through using a disposable column, and the resin was washed with 20 CV of buffer B (20 mM Tris pH 7.4, 300 mM NaCl, 10% glycerol, 1 mM glutamine, 0.05% DDM:CHS or GDN). ASCT2 was eluted from the resin using HRV-3C protease in minimal volume for 2h while rotating. The protein was concentrated using 100 kDa cut-off Amicon concentrator and purified on a Superdex 200 10/300 gel filtration column, pre-equilibrated in buffer C (20 mM Tris pH 7.4, 300 mM NaCl, 10% glycerol, 1 mM glutamine, 0.02% DDM:CHS or GDN). The peak fractions were collected and concentrated using a 100-kDa MWCO Amicon Ultra concentrator, if necessary.

To purify Venus-tagged ASCT2, Strep-Tactin resin was used to capture ASCT2 via the SBP tag. The supernatant with solubilized ASCT2 was incubated with the resin in batch for 1h. Afterward, the unbound proteins were removed in flow-through using a disposable column, and the resin was washed with 20 CVs of buffer B. ASCT2 was eluted from the resin by applying 3 CVs of buffer B supplemented with 5 mM desthiobiotin. Subsequently, the sample was purified on a Superdex 200 10/300 gel filtration column, pre-

equilibrated in buffer C. The peak fractions were collected and concentrated using a 100-kDa MWCO Amicon Ultra concentrator, if necessary.

ASCT2 reconstitution to liposomes and transport assay

Freshly purified Venus-tagged ASCT2 was used for reconstitution into liposomes as previously described[26]. During the reconstitution, one aliquot of E. coli polar lipids and egg PC at a ratio of 3:1 (w/w) and additionally 10% (w/w) cholesterol (Avanti Polar Lipids) was diluted to 4 mg ml^{-1} and destabilized with 10% Triton X-100. Subsequently, lipids were mixed with ASCT2 at a lipid-to-protein ratio of 250:1 (w/w). The assembly was supplemented with 1 mM glutamine. The reconstitution mixture was incubated for 30 min at room temperature (RT), and aliquots of Biobeads were added in four steps: 25 mg ml^{-1} for 30 min at RT, 15 mg ml^{-1} for 1h at 4°C, 19 mg ml^{-1} with overnight incubation at 4 °C, and 29 mg ml^{-1} for 2 h on the next morning at 4 °C. The proteoliposomes were collected by centrifugation (30 min, 442,904×g, 4°C). Finally, proteoliposomes were resuspended in 20 mM Tris-HCl, pH 7.0, aliquoted, flash-frozen in liquid nitrogen, and stored in liquid nitrogen. For the transport assay, an aliquot of proteoliposomes was loaded with 10 mM glutamine and 50 mM NaCl by three freeze-thaw cycles. Liposomes including internal S1-RBD were additionally loaded with 1 µM S1-RBD. Next, the samples were extruded 11 times through a 400 nm polycarbonate filter (Avestin) and ultracentrifuged for 30 min at 4°C and 442,904×g. Finally, proteoliposomes were resuspended in a minimal volume of 20 mM Tris-HCl, pH 7.0, and diluted in buffer containing either 50 mM NaCl alone or additionally 1 µM S1-RBD. Samples were incubated on ice for at least 1h until the start of the transport assay. The uptake was carried out in a water bath at 25°C with constant stirring. The amino acid exchange was initiated by the dilution of proteoliposomes in the external solution containing the final concentration of NaCl at 50 mM, unlabeled glutamine at 50 µM and [^{3}H]-glutamine at 100 nM. The reaction was stopped at indicated time points by diluting an aliquot of solution with proteoliposomes in 2 ml of cold 20 mM Tris-HCl, pH 7.0 and filtering over a 0.45 µm filter (Portran BA-85, Whatman). The filter was washed additionally with 2 ml of cold 20 mM Tris-HCl, pH 7.0. The radioactivity accumulated inside the proteoliposomes, indicative of amino acid exchange, was counted using a PerkinElmer Tri-Carb 2800RT liquid scintillation counter after dissolving the filter in 2 ml of scintillation liquid (Emulsifier Scintillator Plus, PerkinElmer).

Determination of protein orientation in proteoliposomes

A small aliquot of proteoliposomes (corresponding to 2 mg of lipids and 8 µg of protein) was loaded with 10 mM glutamine and 50 mM NaCl by three repeated free-thaw cycles. A control liposome sample included 3C protease. Proteoliposomes were further extruded 11 times through a 400 nm polycarbonate filter (Avestin) and ultracentrifuged for 30 min at 4°C and 442,904×g. Finally, samples were resuspended in a minimal volume of 20 mM Tris-HCl, pH 7.0, and mixed with either an additional amount of 3C protease or nothing else added. After 1h incubation at 4°C, samples were mixed with loading dye and analyzed on SDS-PAGE gel by visualizing fluorescence. The intensity of bands was quantified in ImageJ.

Binding assay

Kinetic characterization of S1-RBD binding to purified ASCT2 was performed using grating-coupled interferometry (GCI) on the WAVEsystem (Creoptix AG, Switzerland). S1-RBD was immobilized on a Protein G PCP-PAG WAVEchip (polycarboxylate quasi-planar surface; Creoptix AG) to a density of 1,700 pg mm^2. ASCT2 purified either in GDN or DDM:CHS (10:1) detergent was injected at concentrations ranging from 200

nM to 1.56 nM (2-fold serial dilution, 8 concentrations). The binding buffer contained 20 mM Tris-HCl pH 7.4, 300 mM NaCl, 1 mM glutamine, and 0.02% detergent GDN or DDM:CHS (10:1). ASCT2 was injected for 200s at a flow rate of 50 µl min^{-1}, and the dissociation was recorded for 600s. All sensograms were recorded at 25°C, and the WAVEcontrol (Creoptix AG) was used for data analysis. Data were double-referenced by subtracting the signals from blank injections and from the reference channel. A Langmuir 1:1 model, including the mass transport, was used for data fitting.

In vitro ASCT2-S1-RBD complex formation in DDM:CHS detergent

ASCT2 was purified as a tagless protein following the method described above using the 3K1K resin. DDM:CHS (10:1) detergent was used throughout ASCT2 purification, complex formation, and pull-down assay. To determine the complex formation in a pull-down assay, ASCT2 (trimer) and S1-RBD were mixed again at a 1:6 molar ratio and incubated with 0.5 ml Ni^{2+} sepharose to capture his-tagged S1-RBD. After 1h incubation at 4℃ and collecting the flow-through, the resin was washed with 10CV of buffer B supplemented with 50 mM imidazole. The protein was eluted with 3CV of buffer B containing 500 mM imidazole. Samples from all subsequent purification steps were analyzed by SDS-PAGE.

In vitro ASCT2-S1-RBD complex formation in GDN detergent

ASCT2 was purified as a Venus-tagged protein following the method described above using the Strep-Tactin resin. GDN detergent was used throughout ASCT2 purification, complex formation, and pull-down assay. Purified ASCT2 (trimer) and S1-RBD were mixed at a 1:4.5 molar ratio, supplemented with 1 mM glutamine, 0.02% GDN, and incubated for 30 min at 4℃ while rotating. After 30 min incubation, the sample was added to 0.5 ml Ni^{2+} sepharose and incubated for another 1h at 4℃ while rotating. Subsequently, the resin was washed with 10CV of buffer B supplemented with 50 mM imidazole. The protein was eluted with 3CV of buffer B containing 500 mM imidazole. Finally, the eluted sample was purified on a Superdex 200 10/300 gel filtration column, preequilibrated in buffer C with 0.02% GDN detergent. Samples from all subsequent purification steps were analyzed by SDS-PAGE and detected by fluorescence and Coomassie staining.

ASCT2-S1-RBD complex formation, cryo-EM sample preparation and data acquisition

Tagless ASCT2 purified in GDN detergent was concentrated to 5 mg ml^{-1} and was used for cryo-EM sample preparation. To obtain ASCT2 and S1-RBD in complex, tagless ASCT2 trimer in GDN and S1-RBD were mixed in a 1:2 molar ratio, incubated for 1h at 4℃ while rotating and subjected to a size-exclusion purification on a Superdex 200 10/300 gel filtration column. The peak fraction was concentrated using a 100-kDa MWCO Amicon Ultra concentrator to ~4.6 mg ml^{-1} concentration and used for cryo-EM sample preparation.

2.8 µl of either sample was applied on holey-carbon cryo-EM grids (Quantifoil, Au R1.2/1.3, 300 mesh) glow-discharged (Edwards Scancoat 6) prior to freezing at 5 mA for 30 s. Grids were blotted for 4s (in case of ASCT2 in GDN) or 3s (in case of ASCT2-S1-RBD sample) in a Vitrobot Mark IV (Thermo Fisher) at 15℃ and 100% humidity, plunged frozen into a liquid ethane-propane mixture, and stored in liquid nitrogen. Cryo-EM data were recorded at the University of Heidelberg (Germany) on a 300-keV Titan Krios Generation 1 microscope equipped with a BioQuantum K3 (Gatan) and using a 20-eV energy slit and a 100 µm objective aperture. The movies were recorded with EPU (Thermo Fisher) operating the K3 camera in super-resolution counting mode and additional binning by two at the nominal magnification of 105,000 (pixel size of 0.836 Å) and an applied defocus range between -0.9 to -1.9 µm. Two exposures per hole were recorded. Each image

was collected during 3.47 s exposure, collecting 76 frames with a total dose of about 60 electrons per Å^2. The targets for data collection were selected based on the ice thickness calculated using an in-house written script[37].

Cryo-EM image processing

ASCT2 in GDN detergent

Data was collected for two days, yielding a total 15,242 micrographs. Preprocessing was carried out in WARP[38] (v1.0.9), including motion correction, dose weighting, and CTF estimation. Micrographs containing ice contamination or with estimated resolution worse than 4Å were excluded, resulting in 13,249 micrographs used for data processing. A total of 5,489,530 particles were automatically picked using crYOLO[39] (v1.7.6) with the general model. Particles were further imported to RELION[40] (v3.1.4) and extracted with 2-fold binning (pixel size 1.672 Å/pix, box size 128 pix). The dataset was then imported to cryoSPARC[41] (v3.3.2) for 2D classification (100 classes, 40 iterations, batch size of, force max over poses disabled), resulting in 2,817,476 particles showing high-resolution features. These particles were imported back to RELION via the PyEM script[42], re-extracted at full pixel size (0.836 Å/pix, box size 256 pix), and subjected to two rounds of 3D classification (five classes, tau fudge 4, C1 symmetry). One class containing well-defined ASCT2 features was selected, comprising 945,238 particles. This subset was further refined through 3D refinement, CTF estimation (beam tilt), and additional round of 3D refinement, yielding a 3.45 Å reconstruction. To improve resolution, a focused 3D classification without alignment was performed using a soft mask around the ASCT2 trimer (10 classes, tau fudge 64, E-step resolution 4Å), resulting in four classes comprising 799,572 particles. These particles underwent Bayesian polishing[43] and CTF refinement (per-micrograph astigmatism) with additional rounds of 3D refinement. The dataset was then imported to cryoSPARC for ab initio reconstruction (five classes) followed by heterogeneous refinement, resulting in 451,550 particles. Iterative non-uniform refinement and CTF refinement resulted in a 2.92 Å reconstruction. Further 3D classification without alignment in RELION identified a subset of 267,040 particles, which was refined in cryoSPARC using non-uniform refinement with applied C3 symmetry, yielding a final map at 2.74 Å resolution.

ASCT2-S1-RBD in GDN detergent

Data was collected in one session, resulting in a total of 6,706 micrographs. WARP[38] (v1.0.9) was used to preprocess data, including motion correction, dose weighting, and CTF estimation. Micrographs showing ice contamination or having an estimated resolution worse than 4Å were excluded, resulting in 5,880 micrographs used for data processing. Particles were selected using a general model with crYOLO[39] (v1.7.6), resulting in a total of 2,704,310 particles. Next, particles were imported to RELION[40] (v3.1.4) and extracted with a box size of 256 pix (pixel size 1.672 Å/pix). The extracted particles were imported to cryoSPARC[41] (v3.3.2) and subjected to 2D classification (100 classes, 20 iterations, batch size of 200). Particles from selected 2D classes (1,465,197 particles) were subjected to ab initio reconstruction (5 classes) and subsequent heterogeneous refinement using ab initio reconstructions as input volumes. The best class contained 633,048 particles, which were refined further using homogenous refinement (C1) and non-uniform refinement (C1). Particles were subjected to another round of ab initio (3 classes) and heterogeneous refinement, resulting in 486,136 particles contributing to the best-resolved class. Those particles were refined using non-uniform refinement in cryoSPARC and afterwards imported to RELION via the PyEM script[42], and subjected to Bayesian polishing, followed by 3D classification without alignment with mask including ASCT2 trimer and S1-

RBD (C1, 5 classes, tau fudge 128). The final set of particles contained 85,256 and yielded a 2.88Å reconstruction (C1) in non-uniform refinement in cryoSPARC.

For both datasets, the final resolution was estimated using the 0.143 gold-standard FSC criterion with a mask excluding the detergent micelle. Local resolution variations were estimated in cryoSPARC. The remote processing 3DFSC server was used to assess the directional resolution anisotropy.

Model building and refinement

The final maps were auto-sharpened with PHENIX[44] and used for model refinement, analysis, and figure preparation. The structure of ASCT2 in the outward-facing state (PDB 8QRO) was fitted into cryo-EM maps in ChimeraX[45]. The S1-RBD model was fitted using PDB 8OUJ. The models were manually adjusted in COOT[46]. The models were subjected to iterative rounds of real-space refinement in PHENIX and rebuilding errors in ISOLDE[47]. Figures were prepared with UCSF ChimeraX. All programs used for image processing and model refinement were accessed through SBGrid[48].

Cell-based functional assays

All the cell-based functional assays were conducted as described previously[23]. The coding sequences of wild-type EAAT1 (Uniprot ID P43003), ASCT1 (Uniprot ID P43007), ASCT2 (Uniprot ID Q15758), and their variants were commercially synthesized by GenScript and cloned with In-Fusion Cloning Kit (TaKaRa) into a previously described gamma-retroviral vector[23]. LTR-containing plasmids were produced in the NEB Stable strain of Escherichia coli. Whole coding sequences were verified by Sanger sequencing.

FE-L cells, lacking endogenous expression of ASCT1 and ASCT2, were transduced to ectopically express EAAT1, ASCT1, ASCT2, and their variants. Each of the transducing viruses was prepared by transfection with Lipofectamine 3000 (ThermoFisher), according to the manufacturer's protocol. 5×10^5 FE-L cells on a P40 dish (TPP, #93040) were co-transfected by 2.5 µg of a mixture containing MLV gagpol, pVSV-G, and the LTR-containing plasmid encoding the selected transporter gene in the ratio 3:1:6. The medium containing transducing viruses was collected 48h after transfection, filtered through a 0.45 µm pore-filter and supplemented with polybrene (4 µg ml^{-1}). A total of 5×10^5 FE-L cells on a P40 dish were infected with 2 mL of the transducing viruses. The transduction efficiency reached 40-90%. The cells were expanded to a P100 dish, and 5 days after the infection, the population of iRFP-positive cells was sorted by fluorescence-activated cell sorting (FACS). The sorting was repeated up to three times to obtain at least a 95%-pure population (**Supplementary Fig. 9a**).

Syncytin-1-pseudotyped virus infections

For the generation of alpharetrovirus pseudotypes, FE-L cells were co-transfected with three plasmids encoding Syncytin-1 with a truncated cytoplasmic domain (stop codon after Leu485), human codon-optimized alpharetroviral gag and pol, and the transduction marker genome pAlpha-SF-mScarlet-wPRE as described previously[23,49,50]. Briefly, 8×10^4 of transporter-expressing cells on a 24-well plate were infected by 0.5 ml of virus-containing supernatant with a multiplicity of infection 0.3. The next day, the medium was exchanged; 2 days postinfection, cells were fixed in 1% paraformaldehyde and analyzed by FACSymphony (BD) flow cytometer. Infected cells were positive for mScarlet. Prior to statistical analysis, data were transformed with complementary log-log regression (Y=ln(-ln(1-fraction of infected cells))) to approximate normal distribution.

Simultaneously, non-infected cells were characterized by flow cytometry for their expression of GFP (protein levels) and iRFP (mRNA levels and sort purity).

Cell-based Syncytin-1 RBD binding assay

The binding of Syncytin-1 to receptor variants was quantified using a fluorescently labeled soluble RBD of Syncytin-1. The fusion protein, hereafter referred to as the fluoroadhesin, consists of the Syncytin-1 RBD followed by the mScarletI3 fluorescent protein[50]. The fluoroadhesin was expressed in HEK293S cells, and conditioned medium containing the secreted protein was collected and used for cell labeling without further purification. For binding assays, cells were washed with PBS and collected using enzyme-free Cell Dissociation Buffer (Gibco). Next, 2.5×10^5 cells expressing individual receptor variants were resuspended in 250 µl of undiluted fluoroadhesin, placed in a tube rotator, and incubated for 60 min at 4 °C. Cells were then washed three times with ice-cold PBS and resuspended in PBS containing Hoechst 33258 to exclude nonviable cells. Samples were analyzed using an LSRII flow cytometer (BD Biosciences), and binding was quantified by measuring the median fluorescence intensity of mScarletI3 within the viable cell population. Prior to statistical analysis, values were log-transformed to approximate a normal distribution.

Syncytin-1 cell-cell fusion assay

The ability of transporter variants to induce Syncytin-1–mediated cell–cell fusion was evaluated using a split-NanoLuc complementation assay. FE-H cells, stably expressing the HiBiT fragment of NanoLuc luciferase, were transfected with a plasmid encoding Syncytin-1 bearing a truncated cytoplasmic tail (stop codon after Leu485). After 24 h, 3×10^5 of transfected FE-H cells were mixed with 3×10^5 of FE-L cells stably expressing the complementary LgBiT fragment together with one of the transporter variants. Mixed cells were seeded into 6-well plates and incubated for 18 h. Finally, cells were harvested using trypsin–EDTA and resuspended in Opti-MEM and transferred to a white 96-well plate in technical triplicate. Luminescence arising from NanoLuc reconstitution in fused cells was quantified using a GloMax Explorer (Promega) after addition of Nano-Glo® Live Cell Reagent (Promega), according to the manufacturer's instructions.

Cell-based amino acid uptake

Amino acid uptake was quantified by measuring the depletion of deuterated amino acids from the culture medium. Cells were seeded in triplicate in 96-well plates at a density of 4×10^4 cells per well. After 24 h, the medium was replaced with glutamine-free DMEM/F-12 (Sigma-Aldrich), and cells were incubated for an additional 24 h. The medium was then exchanged for 140 µl of glutamine-free DMEM/F-12 supplemented with L-Glutamine-2,3,3,4,4-d_5, L-Serine-2,3,3-d_3, and L-Arginine-2,3,3,4,4,5,5-d_7 (CDN Isotopes), each at a final concentration of 100 µM. Culture supernatants were collected after 16 and 24 h of incubation at 37 °C in a humidified atmosphere containing 5% CO_2. Samples were centrifuged (300 × g, 5 min, 4 °C) to remove residual cells, and supernatants were stored at −80 °C until mass spectrometry analysis. Cell-free medium controls were included and processed in parallel.

Media samples were thawed, vortexed, and centrifuged at 15,000×g for 15 min at 6 °C. A 50 µL aliquot of the supernatant was transferred to a 384-well plate (Echo MS-qualified, Labcyte). Well plates were centrifuged at 2,000×g for 5 min (Centrifuge 5810 R, Eppendorf) and shaken at 1,000 rpm for 2 min (ThermoMixer C, Eppendorf). Acoustic Ejection Mass Spectrometry (AEMS) was performed using an Echo MS system coupled to a Triple Quad 6500+ mass spectrometer (SCIEX) via an Open Port Interface (OPI). The system was

operated in Multiple Reaction Monitoring (MRM) mode using SciexOS software (3.4). MRM transitions for the labeled standards (L-Glutamine-2,3,3,4,4-d_5, L-Serine-2,3,3-d_3, and L-Arginine-2,3,3,4,4,5,5-d_7; CDN Isotopes) were optimized to ensure maximum intensity and absence of matrix interference from the DMEM/F-12 medium (**Supplementary Table 5**).

Contactless sampling was performed by ejecting a total of 5 nL (in 2.5 nL increments) directly into the mobile phase (20% MeOH, 0.1% formic acid, and 5 mM 1,1,1,3,3,3-hexafluoro-2-propanol) at a flow rate of 390 µL/min. The ESI source was operated in positive mode: ion source gas 1 (90 psi), gas 2 (60 psi), curtain gas (20 psi), temperature (350 °C), spray voltage (5000 V), and CAD gas (9 psi).

Prior to statistical analysis, values relative to cell-free medium were log-transformed to approximate a normal distribution.

Statistical evaluation

Statistical tests were performed in GraphPad Prism v10.6.1 and details are provided in figure legends. P-values are indicated as follows: $*$, $P<0.05$; $**$, $P<0.01$; $***$, $P<0.001$; $****$, $P<0.0001$.

Acknowledgements

We want to thank P. Drougkas for help with cryo-EM data collection and advice on image processing, M. Punter for maintenance of the image processing cluster, and M. Stuart for supportive discussions on cryo-EM. We are grateful to L. Jech and D. Kucerova for laboratory support. We also thank all members of Membrane Enzymology, Paulino group, and Hejnar lab for the insightful work discussions. We thank Z. Cimburek and M. Sima from the Service Laboratory of Flow Cytometry at the Institute of Molecular Genetics of the Czech Academy of Sciences for excellent technical assistance with cell sorting and flow cytometry.

We would like to acknowledge access to the cryo-EM infrastructure and support provided by the Cryo-EM Network at the Heidelberg University (HDcryoNet), which is funded and supported by the German Research Foundation (DFG), the Federal Ministry of Education and Research (BMBF), and the Ministry of Science , Research and the Arts Baden-Württemberg, among others, within the framework of the Excellence Strategy of the Federal and State Governments of Germany.

D.J.S. acknowledges funding from the Dutch Research Council (Nederlandse Organisatie voor Wetenschappelijk Onderzoek, NWO; Open Competition grant OCENW.M.21.248). This work was also supported by the Czech Academy of Sciences (institutional support RVO: 61388963) and the National Institute of Virology and Bacteriology (Programme EXCELES, Project No. LX22NPO5103), funded by the European Union - Next Generation EU. K.S. acknowledges the support from the Czech Science Foundation (Project No. 26-22793O).

Authors Contribution

All authors designed the research. M.S. cloned and generated the baculovirus for S1-RBD expression, established the initial expression and purification protocol, and performed initial S1-RBD expression and purification experiments. A.B. performed ASCT2 protein expression and purification, expressed S1-RBD and further optimized its purification, tested all complex formation strategies, processed cryo-EM data and determined the structure. J.R. collected cryo-EM data for ASCT2-S1-RBD sample. A.B. and K.S. analyzed the structure and selected residues for mutagenesis. K.S. and K.T. designed all ASCT2 and ASCT1 mutants, which were cloned by L.P. K.S. generated all ASCT2- and ASCT1-expressing cell lines, performed infection assays with Syncytin-1-pseudotyped virus, and analyzed the data. K.T. prepared Syncytin-1 virus stocks, expressed the S1-RBD fluoroadhesin, and performed fluoroadhesin binding assays, M.T. performed fusion assays. M.T. and A.J. performed amino acid uptake assays. A.B., K.S., D.J.S., and K.T. prepared the manuscript with input from all authors.

Data Availability

The cryo-EM maps have been deposited in the Electron Microscopy Data Bank (EMDB) under accession codes EMD-57883 (ASCT2 in GDN) and EMD-57882 (ASC T2-S1-RBD complex). The atomic coordinated have been deposited in the Protein Data Bank (PDB) under accession codes 30LK (ASCT2 in GDN) and 30LJ (ASCT2-S1-RBD complex). Raw cryo-EM data is currently deposited in the Electron Microscopy Public Image Archive (EMPIAR).

References

1. Gifford, R. & Tristem, M. The Evolution, Distribution and Diversity of Endogenous Retroviruses. *Virus Genes* **26**, 291–315 (2003).
2. Blond, J. L. *et al.* An envelope glycoprotein of the human endogenous retrovirus HERV-W is expressed in the human placenta and fuses cells expressing the type D mammalian retrovirus receptor. *J Virol* **74**, 3321–3329 (2000).
3. Matoušková, M., Blažková, J., Pajer, P., Pavlíček, A. & Hejnar, J. CpG methylation suppresses transcriptional activity of human syncytin-1 in non-placental tissues. *Experimental Cell Research* **312**, 1011–1020 (2006).
4. Trejbalová, K. *et al.* Epigenetic regulation of transcription and splicing of syncytins, fusogenic glycoproteins of retroviral origin. *Nucleic Acids Research* **39**, 8728–8739 (2011).
5. Mi, S. *et al.* Syncytin is a captive retroviral envelope protein involved in human placental morphogenesis. *Nature* **403**, 785–9 (2000).
6. Dupressoir, A. *et al.* Syncytin-A knockout mice demonstrate the critical role in placentation of a fusogenic, endogenous retrovirus-derived, envelope gene. *Proc. Natl. Acad. Sci. U.S.A.* **106**, 12127–12132 (2009).
7. Dupressoir, A. *et al.* A pair of co-opted retroviral envelope *syncytin* genes is required for formation of the two-layered murine placental syncytiotrophoblast. *Proc. Natl. Acad. Sci. U.S.A.* **108**, (2011).
8. Funk, M. *et al.* Capture of a Hyena-Specific Retroviral Envelope Gene with Placental Expression Associated in Evolution with the Unique Emergence among Carnivorans of Hemochorial Placentation in Hyaenidae. *J Virol* **93**, e01811-18 (2019).
9. Cheynet, V. *et al.* Synthesis, assembly, and processing of the Env ERVWE1/syncytin human endogenous retroviral envelope. *J Virol* **79**, 5585–93 (2005).
10. Hogan, V. & Johnson, W. E. Unique Structure and Distinctive Properties of the Ancient and Ubiquitous Gamma-Type Envelope Glycoprotein. *Viruses* **15**, 274 (2023).
11. Sinha, A. & Johnson, W. E. Retroviruses of the RDR superinfection interference group: ancient origins and broad host distribution of a promiscuous Env gene. *Current Opinion in Virology* **25**, 105–112 (2017).
12. Tailor, C. S., Nouri, A., Zhao, Y., Takeuchi, Y. & Kabat, D. A sodium-dependent neutral-amino-acid transporter mediates infections of feline and baboon endogenous retroviruses and simian type D retroviruses. *J Virol* **73**, 4470–4 (1999).
13. Marin, M., Tailor, C. S., Nouri, A. & Kabat, D. Sodium-dependent neutral amino acid transporter type 1 is an auxiliary receptor for baboon endogenous retrovirus. *J Virol* **74**, 8085–93 (2000).
14. Lavillette, D. *et al.* The envelope glycoprotein of human endogenous retrovirus type W uses a divergent family of amino acid transporters/cell surface receptors. *J Virol* **76**, 6442–52 (2002).
15. Utsunomiya-Tate, N., Endou, H. & Kanai, Y. Cloning and functional characterization of a system ASC-like Na+-dependent neutral amino acid transporter. *J Biol Chem* **271**, 14883–14890 (1996).
16. Broer, A. *et al.* The astroglial ASCT2 amino acid transporter as a mediator of glutamine efflux. *J Neurochem* **73**, 2184–94 (1999).

17. Grewer, C. *et al.* Individual subunits of the glutamate transporter EAAC1 homotrimer function independently of each other. *Biochemistry* **44**, 11913–23 (2005).
18. Erkens, G. B., Hanelt, I., Goudsmits, J. M., Slotboom, D. J. & van Oijen, A. M. Unsynchronised subunit motion in single trimeric sodium-coupled aspartate transporters. *Nature* **502**, 119–23 (2013).
19. Garaeva, A. A. *et al.* Cryo-EM structure of the human neutral amino acid transporter ASCT2. *Nat Struct Mol Biol* **25**, 515–521 (2018).
20. Marin, M., Lavillette, D., Kelly, S. M. & Kabat, D. N-linked glycosylation and sequence changes in a critical negative control region of the ASCT1 and ASCT2 neutral amino acid transporters determine their retroviral receptor functions. *J Virol* **77**, 2936–45 (2003).
21. Khare, S. *et al.* Receptor-recognition and antiviral mechanisms of retrovirus-derived human proteins. *Nat Struct Mol Biol* https://doi.org/10.1038/s41594-024-01295-6 (2024) doi:10.1038/s41594-024-01295-6.
22. Pavlo Stehantsev, A. S., Mariia Nemchinova, Nanda Gowtham Aduri, Siewert J. Marrink, Cornelius Gati, Albert Guskov. A structural view onto disease-linked mutations in the human neutral amino acid exchanger ASCT1. *Computational and Structural Biotechnology Journal* **19**, (2021).
23. Štafl, K. *et al.* Receptor usage of Syncytin-1: ASCT2, but not ASCT1, is a functional receptor and effector of cell fusion in the human placenta. *Proc. Natl. Acad. Sci. U.S.A.* **121**, e2407519121 (2024).
24. Zingler, K. & Young, J. A. Residue Trp-48 of Tva is critical for viral entry but not for high-affinity binding to the SU glycoprotein of subgroup A avian leukosis and sarcoma viruses. *J Virol* **70**, 7510–7516 (1996).
25. Garaeva, A. A., Guskov, A., Slotboom, D. J. & Paulino, C. A one-gate elevator mechanism for the human neutral amino acid transporter ASCT2. *Nat Commun* **10**, 3427 (2019).
26. Borowska, A. M. *et al.* Structural basis of the obligatory exchange mode of human neutral amino acid transporter ASCT2. *Nat Commun* **15**, 6570 (2024).
27. Knöfler, M. *et al.* Human placenta and trophoblast development: key molecular mechanisms and model systems. *Cell. Mol. Life Sci.* **76**, 3479–3496 (2019).
28. Sauer, D. *et al.* Amino acid and viral binding by the high-affinity Cationic Amino acidTransporter 1 (CAT1) from Mus musculus. Preprint at https://doi.org/10.21203/rs.3.rs-4673967/v1 (2024).
29. Cirri, E. *et al.* Consensus designs and thermal stability determinants of a human glutamate transporter. *Elife* **7**, (2018).
30. Stafl, K. *et al.* Heterologous avian system for quantitative analysis of Syncytin-1 interaction with ASCT2 receptor. *Retrovirology* **18**, 15 (2021).
31. Yoo, H. C. *et al.* A Variant of SLC1A5 Is a Mitochondrial Glutamine Transporter for Metabolic Reprogramming in Cancer Cells. *Cell Metab* **31**, 267-283 e12 (2020).
32. Console, L., Scalise, M., Tarmakova, Z., Coe, I. R. & Indiveri, C. N-linked glycosylation of human SLC1A5 (ASCT2) transporter is critical for trafficking to membrane. *Biochim Biophys Acta* **1853**, 1636–45 (2015).
33. Weissmann, F. *et al.* biGBac enables rapid gene assembly for the expression of large multisubunit protein complexes. *Proc. Natl. Acad. Sci. U.S.A.* **113**, (2016).
34. Morales-Perez, C. L., Noviello, C. M. & Hibbs, R. E. Manipulation of Subunit Stoichiometry in Heteromeric Membrane Proteins. *Structure* **24**, 797–805 (2016).

35. Geertsma, E. R. & Dutzler, R. A versatile and efficient high-throughput cloning tool for structural biology. *Biochemistry* **50**, 3272–8 (2011).
36. Goehring, A. *et al.* Screening and large-scale expression of membrane proteins in mammalian cells for structural studies. *Nat Protoc* **9**, 2574–2585 (2014).
37. Rheinberger, J., Oostergetel, G., Resch, G. P. & Paulino, C. Optimized cryo-EM data-acquisition workflow by sample-thickness determination. *Acta Crystallogr D Struct Biol* **77**, 565–571 (2021).
38. Tegunov, D. & Cramer, P. Real-time cryo-electron microscopy data preprocessing with Warp. *Nat Methods* **16**, 1146–1152 (2019).
39. Wagner, T. *et al.* SPHIRE-crYOLO is a fast and accurate fully automated particle picker for cryo-EM. *Commun Biol* **2**, 218 (2019).
40. Zivanov, J. *et al.* New tools for automated high-resolution cryo-EM structure determination in RELION-3. *eLife* **7**, e42166 (2018).
41. Punjani, A., Rubinstein, J. L., Fleet, D. J. & Brubaker, M. A. cryoSPARC: algorithms for rapid unsupervised cryo-EM structure determination. *Nat Methods* **14**, 290-+ (2017).
42. Asarnow, D., Palovcak, E. & Cheng, Y. asarnow/pyem: UCSF pyem v0.5. Zenodo https://doi.org/10.5281/ZENODO.3576630 (2019).
43. Zivanov, J., Nakane, T. & Scheres, S. H. W. A Bayesian approach to beam-induced motion correction in cryo-EM single-particle analysis. *IUCrJ* **6**, 5–17 (2019).
44. Adams, P. D. *et al. PHENIX*: a comprehensive Python-based system for macromolecular structure solution. *Acta Crystallogr D Biol Crystallogr* **66**, 213–221 (2010).
45. Goddard, T. D. *et al.* UCSF ChimeraX: Meeting modern challenges in visualization and analysis. *Protein Science* **27**, 14–25 (2018).
46. Emsley, P. & Cowtan, K. *Coot*: model-building tools for molecular graphics. *Acta Crystallogr D Biol Crystallogr* **60**, 2126–2132 (2004).
47. Croll, T. I. *ISOLDE*: a physically realistic environment for model building into low-resolution electron-density maps. *Acta Crystallogr D Struct Biol* **74**, 519–530 (2018).
48. Morin, A. *et al.* Collaboration gets the most out of software. *eLife* **2**, e01456 (2013).
49. Suerth, J. D., Maetzig, T., Galla, M., Baum, C. & Schambach, A. Self-Inactivating Alpharetroviral Vectors with a Split-Packaging Design. *J Virol* **84**, 6626–6635 (2010).
50. Krchlikova, V. *et al.* Inhibition of placental trophoblast fusion by guanylate-binding protein 5. *Sci. Adv.* **11**, eadt5388 (2025).

Supplementary Files

This is a list of supplementary files associated with this preprint. Click to download.

- syncytinmanuscriptsupplementaryfiguresfinal.pdf
- ASCT2glnGDNvalidationreport.pdf
- ASCT2S1RBDGDNvalidationreport.pdf